Draft version April 28, 2023
Typeset using LaTeX **twocolumn** style in AASTeX631

Constrain the Dark Matter Distribution of Ultra-diffuse Galaxies with Globular-Cluster Mass Segregation: A Case Study with NGC5846-UDG1

Jinning Liang [1,2] Fangzhou Jiang [2,3,4,*] Shany Danieli [5] Andrew Benson [3] and Phil Hopkins [4]

[1] School of Physics and Technology, Wuhan University, Wuhan, Hubei 430072, China
[2] Kavli Institute for Astronomy and Astrophysics, Peking University, Beijing 100871, China
[3] Carnegie Observatories, 813 Santa Barbara Street, Pasadena, CA 91101, USA
[4] TAPIR, California Institute of Technology, Pasadena, CA 91125, USA
[5] Department of Astrophysical Sciences, 4 Ivy Lane, Princeton University, Princeton, NJ 08544

ABSTRACT

The properties of globular clusters (GCs) contain valuable information of their host galaxies and dark-matter halos. In the remarkable example of ultra-diffuse galaxy, NGC5846-UDG1, the GC population exhibits strong radial mass segregation, indicative of dynamical-friction-driven orbital decay, which opens the possibility of using imaging data alone to constrain the dark-matter content of the galaxy. To explore this possibility, we develop a semi-analytical model of GC evolution, which starts from the initial mass function, the initial structure-mass relation, and the initial spatial distribution of the GC progenitors, and follows the effects of dynamical friction, tidal evolution, and two-body relaxation. Using Markov Chain Monte Carlo, we forward-model the GCs in a NGC5846-UDG1-like potential to match the observed GC mass, size, and spatial distributions, and to constrain the profile of the host halo and the origin of the GCs. We find that, with the assumptions of zero mass segregation when the star clusters were born, NGC5846-UDG1 is dark-matter poor compared to what is expected from stellar-to-halo-mass relations, and its halo concentration is low, irrespective of having a cuspy or a cored halo profile. Its GC population has an initial spatial distribution more extended than the smooth stellar distribution. We discuss the results in the context of scaling laws of galaxy-halo connections, and warn against naively using the GC-abundance-halo-mass relation to infer the halo mass of UDGs. Our model is generally applicable to GC-rich dwarf galaxies, and is publicly available at https://github.com/JiangFangzhou/GCevo.

Keywords: Galaxy dark matter halos (1880) — Globular star clusters (656) — Dynamical friction (422) — Dwarf galaxies (416)

1. INTRODUCTION

Ultra-diffuse galaxies (UDGs) triggered a frenzy of studies in recent years in the contexts of both understanding the formation of extreme galaxies and testing cosmology (see e.g., the review by Sales et al. 2020, and the references therein). Numerical and semi-analytical simulations suggest that UDGs can form via supernovae-driven gas outflows, which transform their hosting dark-matter halos from cuspy to cored together with puffing up their stellar distribution (e.g., Di Cintio et al. 2017; Chan 2019; Jiang et al. 2019), while some UDGs can also populate halos of high specific angular momentum (e.g., Rong et al. 2017; Amorisco & Loeb 2016; Benavides et al. 2022). The formation of UDGs is also suggested to be facilitated in dense environments, via tidal heating (Jiang et al. 2019; Carleton et al. 2019; Liao et al. 2019) and passive stellar-population dimming (Tremmel et al. 2020). Despite all these theoretical efforts, there are still several aspects of UDGs that remain intriguing. Notably, UDGs on average have more globular clusters (GCs) than normal galaxies of similar stellar mass (van Dokkum et al. 2016, 2017; Lim et al. 2018; Forbes et al. 2020). There exists an empirical relation between GC abundance and dark-matter (DM) halo mass, valid over almost five dex of virial mass for normal galaxies (Hudson et al. 2014; Harris et al. 2015, 2017; Burkert & Forbes 2020). If this relation holds for UDGs, then a higher-than-average GC abundance implies that the host DM halo is overly massive for the stellar mass. In

* Corresponding author: fangzhou.jiang@pku.edu.cn

contrast, some UDGs seem to be DM deficient, based on their GC or gas kinematics (van Dokkum et al. 2018, 2019; Danieli et al. 2019; Guo et al. 2020), which poses a challenge to the standard picture where galaxy formation takes place in DM halos that dominate the mass budget. Hence, to understand the GC populations of UDGs takes center stage in understanding UDG formation in a cosmological context. Notably, the abundance, the spatial distribution, and the kinematics of GCs all contain information of the DM distribution of their hosting UDG.

The galaxy NGC5846-UDG1 (UDG1 hereafter) serves as a remarkable example (Müller et al. 2020; Forbes et al. 2021; Danieli et al. 2022b; Bar et al. 2022). On the one hand, it hosts a surprisingly large population of GCs (of ~ 50 within two stellar effective radii) for its stellar mass of $\sim 10^8 M_\odot$. This translates to an overly massive DM halo of $\sim 10^{11} M_\odot$ assuming the Harris et al. relation (Forbes et al. 2021). On the other hand, the GC population of UDG1 shows a strong radial mass segregation (Bar et al. 2022), with more massive GCs lying closer to the center of the galaxy. The mass segregation can be most naturally interpreted as a manifestation of orbital decay caused by dynamical friction (DF), because the strength of DF scales strongly with the perturber mass. And if DF causes the mass segregation, the halo mass should be much lower, because the timescale of orbital decay depends on the perturber-to-host mass ratio (m/M), such that it is shorter than the dynamical timescale of the host galaxy only if $m/M \gtrsim 1/100$ (e.g. Boylan-Kolchin et al. 2008). That is, for a GC of mass $m \sim 10^6 M_\odot$, the host halo cannot be orders of magnitudes more massive than the stellar component ($\sim 10^8 M_\odot$) in order to have sufficient orbital decay and mass segregation. Admittedly, this mass-ratio argument was originally made for satellite galaxies entering the host at orbital energies comparable to that of a circular orbit at the virial radius, so the GCs near the host center and thus with much lower orbital energy in principle allow for smaller mass ratios (and therefore larger host halo masses). This, however, requires more detailed modeling that considers the locations of the GCs at birth and the density profile of the host. The strikingly different halo-mass estimates based on the aforementioned two perspectives highlights the importance of such models.

In this work, we first present a semi-analytical model of GC evolution in a composite host potential consisting of stellar and DM distributions. While generally applicable to any dwarf galaxy that exhibits a radial trend of its GC properties, here this model is applied to UDG1 as a proof of concept, showing that the observed mass segregation, together with the other information of the GCs available in the imaging data, can be used to constrain the DM halo. As a major improvement over previous studies which also attribute the GC mass segregation to dynamical friction (Bar et al. 2022; Modak et al. 2022), a more physical model of the evolution of star clusters under the influence of tidal interactions with the host galaxy and the internal two-body relaxation is considerted. Tidal interactions and two-body relaxation drive mass loss and structural changes of the GCs, thus affecting the orbital evolution and the spatial distribution in a subtle but important way, as we will discuss below. When combined with parameter inference tools, this model enables using imaging data alone, without costly kinematics observations, to statistically constrain the DM distribution of the host galaxy. Additionally, the extreme limit of GC mass segregation is the complete orbital decay of massive GCs to the galaxy center, which is a viable way of forming dense nuclear star clusters as observed in nucleated low-surface-brightness galaxies (Lim et al. 2018; Greco et al. 2018; Sánchez-Janssen et al. 2019; Iodice et al. 2020; Marleau et al. 2021). Our method is therefore also potentially useful in this context.

This work is organized as follows. In Section 2, we introduce our model of GC evolution, and present the workflow of forward modeling the GC population and inferring the host DM profile. In Section 3, we use the observed GC statistics of UDG1 to constrain the model parameters, including the DM halo mass and concentration, as well as the characteristic spatial scale of the initial distribution of the GCs which may shed light upon the origin of the GCs. In Section 4, we compare the model predictions and kinematics observations, discuss the key distinction between a cuspy halo profile versus a cored profile regarding star-cluster statistics, compare our model to simplistic models that ignore the physics of GC mass and structural evolution, and also comment on potential future developments of this methodology. We draw our conclusions in Section 5.

Throughout, we define the virial radius of the hosting DM halo as the radius within which the average density is $\Delta = 200$ times the critical density for closure, and adopt a flat cosmology with the present-day matter density $\Omega_\mathrm{m} = 0.3$, baryonic density $\Omega_\mathrm{b} = 0.0465$, dark energy density $\Omega_\Lambda = 0.7$, a power spectrum normalization $\sigma_8 = 0.8$, a power-law spectral index of $n_s = 1$, and a Hubble parameter of $h = 0.7$. We use r, R, and l to indicate the three-dimensional galactocentric radius, the projected galactocentric radius, and star-cluster-centric radius, respectively; and denote the mass of a star cluster and that of the host galaxy by m and M, respectively.

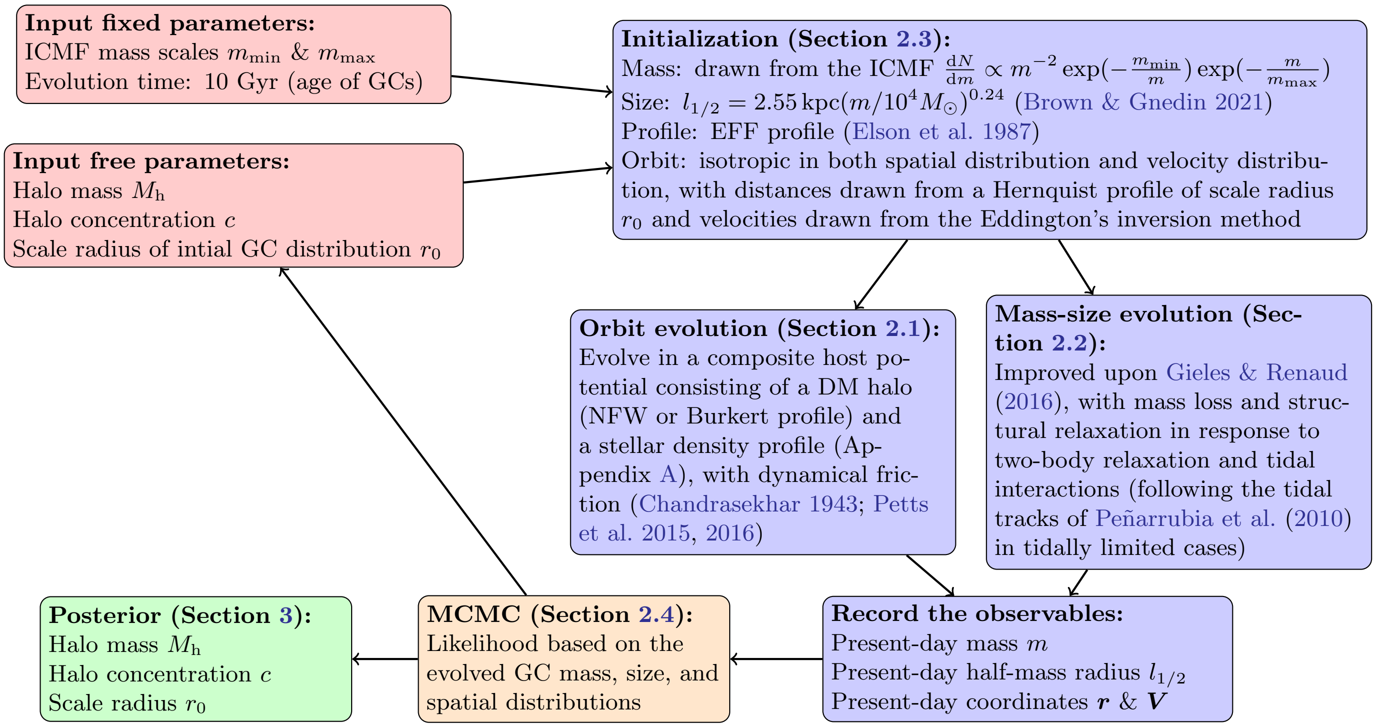

Figure 1. Model workflow. The `SatGen` (Jiang et al. 2021) semi-analytical framework for galaxy evolution provides the backbone of this model. The star-cluster-specific prescriptions are summarized here and detailed in Section 2.

2. METHODOLOGY

In this section, we first introduce a dynamical model that describes the evolution of GCs in a composite host potential consisting of dark matter and stars. This model considers the orbital evolution of GCs under the influence of dynamical friction (DF), allowing for the dependence of the strength of DF on the local density profile of the host potential following the recipe of Petts et al. (2015). The GCs evolve in mass and structure in response to the internal two-body relaxation and the varying tidal effects along the orbits. We then lay out the model assumptions, including the initial star-cluster mass function, the initial structure of young star clusters, the initial spatial distribution of the star clusters, and the assumptions about the host potential. With these assumptions, the model self-consistently evolves a population of GCs, predicting their evolved masses, sizes, and spatial distribution, which are then compared to those of the observed GC population. Finally, we combine the model with a Markov Chain Monte Carlo (MCMC) inference tool, to derive constraints on the DM halo of the target galaxy.

Fig. 1 presents a schematic flowchart that summarizes all the components of our framework, and could be a good starting place for readers who wish to skip the technical details to the results.

2.1. *Orbit Evolution*

To follow the orbit of a GC, we solve the equation of motion,

$$\ddot{\boldsymbol{r}} = -\nabla\Phi + \boldsymbol{a}_{\rm DF}, \tag{1}$$

where $\boldsymbol{r}$ is the position vector, Φ is the gravitational potential, and $\boldsymbol{a}_{\rm DF}$ is the acceleration due to DF, given by (Chandrasekhar 1943)

$$\boldsymbol{a}_{\rm DF} = -4\pi G^2 m \sum_i \ln\Lambda_i \rho_i(\boldsymbol{r}) F(<V_i)\frac{\boldsymbol{V}_i}{V_i^3}. \tag{2}$$

Here, the summation is over different components of the host potential (i = DM, stars), m is the mass of the GC, $\ln\Lambda_i$ is the Coulomb logarithm, $\boldsymbol{V}_i$ is the relative velocity of the GC with respect to component i, and $F(<V_i)$ is fraction of particles that contribute to DF, which, under the assumption of a Maxwellian distribution, is given by $F(<V_i) = {\rm erf}(X_i) - (2X_i/\sqrt{\pi})e^{-X_i^2}$, where $X_i = V_i/(\sqrt{2}\sigma_i)$, with σ_i the one-dimensional velocity dispersion of component i at position $\boldsymbol{r}$.

In the idealized Chandrasekhar picture of dynamical friction, the perturber travels across an infinite homogeneous isotropic medium, and Λ is defined as $b_{\rm max}/b_{\rm min}$, with $b_{\rm max}$ and $b_{\rm min}$ the maximum and minimum impact parameters, respectively. For perturbers orbiting a galaxy, which is not a uniform medium, the Chandrasekhar DF treatment is used as an approximation, where $b_{\rm max}$ is of the order of the characteristic size of the host system, and $b_{\rm min}$ is the larger of the impact parameter for a 90-degree deflection and the size of the perturber (Binney & Tremaine 2008). In semi-analytical models of satellite-galaxy evolution, it is a common practice to simply assume $\ln\Lambda \sim \ln(M/m)$, where M/m is the mass ratio of the host and the satellite, as the virial radius of a gravitationally bound structure scales with the virial mass (see e.g., Gan et al. 2010, and the references therein). Even constant Coulomb logarithms of $\ln\Lambda \sim 3$ are widely adopted, as major and minor mergers ($M/m \lesssim 10$) contributes to the bulk of the surviving satellite galaxies. Hence, for the purpose of studying satellite galaxies, where typically the focus is not on the orbital evolution of individual perturbers but on the overall satellite statistics, the simplistic forms of Coulomb logarithm such as $\ln\Lambda \sim \ln(M/m)$ and ~ 3 are reasonable (Green et al. 2021). However, for our purpose here, i.e., to use the GC mass segregation to constrain the dynamical mass distribution, the details of individual orbits are important and thus the simplistic Coulomb logarithms for satellite galaxies may be problematic. For example, $\ln\Lambda \sim \ln(M/m)$ would be very high for GCs and the orbital decay would be unrealistically strong.

Hence, following the more detailed treatment of Petts et al. (2015), we choose $b_{\rm max}$ to be

$$b_{\rm max}(r) = \min\left\{\frac{r}{\gamma(r)}, r\right\} \tag{3}$$

where $\gamma(r) \equiv -{\rm d}\ln\rho/{\rm d}\ln r$ is the local logarithmic density slope of the host potential, and choose $b_{\rm min}$ as

$$b_{\rm min} = \max\left\{l_{1/2}, \frac{Gm}{V^2}\right\}, \tag{4}$$

where $l_{1/2}$ is the half-mass radius of the GC. [1] As such, $b_{\rm max}$ is a length scale over which the density is approximately constant (Just et al. 2011). To deal with the cases of $b_{\rm max} \sim b_{\rm min}$, which can happen when a GC approaches the center of the host, we use the original Chandrasekhar result for the Coulomb logarithm $0.5\ln(\Lambda^2+1)$ in place of the $\ln\Lambda$ in eq. (2). These choices empirically account for the core-stalling effect (Goerdt et al. 2006; Read et al. 2006; Inoue 2009; Kaur & Sridhar 2018), the phenomenon that the DF acceleration decreases and the orbital decay stalls when the perturber approaches a flat density core – because in the density core, $\gamma(r) \sim 0$, $b_{\rm max} \sim b_{\rm min} \sim r$ and $\ln(\Lambda^2 + 1) \sim 0$.

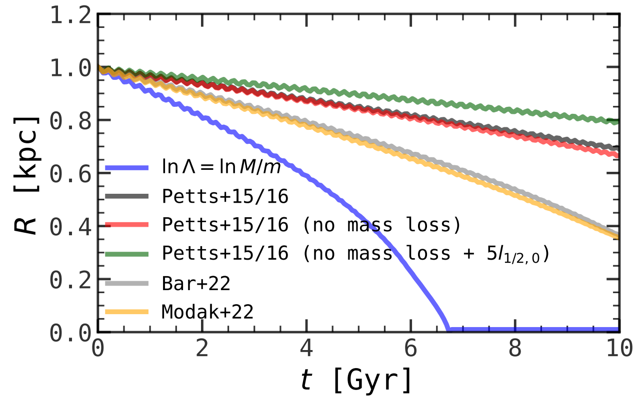

Figure 2. Illustration of the effects of different prescriptions of the Coulomb logarithm in the Chandrasekhar DF formula on the orbit evolution of a star cluster. Here, we release a GC of an initial mass of $m = 10^5 M_\odot$ on a circular orbit of $R = 1\,{\rm kpc}$ in a host NFW halo of $M_{\rm h} = 10^{9.5} M_\odot$ and $c = 10$. The black line stands for the result using our fiducial model of GC evolution (Section 2.2) and the Petts et al. Coulomb logarithm (Section 2.1). The other lines represent the results from varying certain aspect, using, e.g., the same fiducial Λ but with no mass loss (red), the same Λ but with no mass loss and with the GC size boosted by 5x (green), the fiducial evolution model but with a Λ widely assumed for satellite-galaxy evolution (blue). Note that, first, the GC mass-size evolution affects orbital evolution via the DF treatment; second, the Petts et al. Coulomb logarithm gives much weaker orbital decay than the simplistic $\ln\Lambda = \ln M/m$; third, the Bar et al. and Modak et al. recipes, which are simplified versions of Petts et al. that ignore the GC size in $b_{\rm min}$, result in stronger DF than the full treatment.

Fig. 2 compares the orbital evolution for different prescriptions of the Coulomb logarithm as well as for different GC mass evolution models. Focusing on the comparison of the blue and black lines, we can see that the simplistic Coulomb logarithm of $\ln(M/m)$ yields significantly stronger orbital decay than the more accurate Petts et al. treatment, which has been well calibrated against numerical simulations.

We also note that in two previous studies that are highly relevant, Bar et al. (2022) and Modak et al. (2022), the Coulomb logarithms were chosen to be simplified variants of what we use here. The key difference is that their models do not follow the size evolution of the GCs, so their $b_{\rm min}$ are effectively $\sim Gm/V^2$, which is usually a factor of a few smaller than $l_{1/2}$, making the Coulomb logarithm larger and DF stronger than the full treatment, as also illustrated in Fig. 2. We will elaborate on the comparisons of our model with these models in Section 4.3.

[1] In practice, we do not distinguish the half-mass radius from the effective radius (i.e., 2D half-light radius), which is provided by the observational data for the GCs in UDG1 and the size-mass relation of young star clusters (Brown & Gnedin 2021, as will be discussed in Section 2.3).

2.2. *A unified model of mass-size evolution*

GCs are compact objects that are more resilient to the environmental processes than more diffuse substructures of a galaxy such as DM substructures and gas clouds. This is largely why in previous studies of GC mass segregation, the mass evolution of the GCs was treated simplistically and the structural evolution of the GCs were completely ignored (Dutta Chowdhury et al. 2020; Bar et al. 2022; Modak et al. 2022). However, when dealing with the long-term evolution over the age of the clusters ($\sim 10\,\mathrm{Gyr}$), the tidal interactions between the GCs and the host galaxy, especially near the center of the host, can result in non-trivial mass and structural change. In the meantime, GCs are internally collisional, and thus lose mass and expand due to the evaporation of stars. This is relevant even in low-density environments. The combination of the external tidal effects and the internal two-body relaxation may result in non-linear mass loss and structural change, which, in turn, affects the orbital evolution, since the DF acceleration depends on the mass and structure of the perturber, as discussed in Section 2.1. Additionally, the imaging data of the GCs in nearby low-surface-brightness galaxies can be high-resolution enough to provide information about the internal structure of the GCs (van Dokkum et al. 2018). This potentially also contains valuable information of the dynamics besides the mere mass and spatial distribution. For all these reasons, we model the mass-size evolution of the GCs.

Our model of GC mass-size evolution adopts a similar formalism as that of Gieles & Renaud (2016, GR16) but is different in two important aspects. First, GR16 focused on the evolution of newly born star clusters younger than 100 Myr in the vicinity of their birth places, and therefore the dominant tidal effect is the repeated impulsive encounters with giant molecular clouds in the clumpy inter stellar medium surrounding the clusters. Here, we trace the long-term evolution of star clusters over cosmological timescales, and therefore we focus more on the tidal interactions with the background potential. Second, because of the short-term nature, the GR16 model assumes that two-body relaxation causes no mass loss, whereas here we cannot ignore the mass loss from two-body relaxation over the age of the GCs.

We start by differentiating the binding energy $E \propto -Gm^{5/3}\rho_{1/2}^{1/3}$ of a GC, and express the derivative in terms of the mass, m, and the average density within the half-mass radius, $\rho_{1/2}$:

$$\frac{\mathrm{d}E}{E} = \frac{5}{3}\frac{\mathrm{d}m}{m} + \frac{1}{3}\frac{\mathrm{d}\rho_{1/2}}{\rho_{1/2}}. \tag{5}$$

Both tidal interactions and two-body relaxation contribute to the energy increase $\mathrm{d}E$ and the mass loss $\mathrm{d}m$, so we distinguish their contributions by denoting $\mathrm{d}E$ and $\mathrm{d}m$ in two terms with subscripts "t" and "r", respectively,

$$\frac{\mathrm{d}E_\mathrm{t} + \mathrm{d}E_\mathrm{r}}{E} = \frac{5}{3}\frac{\mathrm{d}m_\mathrm{t} + \mathrm{d}m_\mathrm{r}}{m} + \frac{1}{3}\frac{\mathrm{d}\rho_{1/2}}{\rho_{1/2}}. \tag{6}$$

Following GR16, we introduce a parameter f_t to relate the mass loss to the tidal heating from the interactions with the host potential:

$$\frac{\mathrm{d}m_\mathrm{t}}{m} = f_\mathrm{t}\frac{\mathrm{d}E_\mathrm{t}}{E}. \tag{7}$$

Similarly, we define an f_r parameter that relates mass loss to the internal heating due to two-body relaxation:

$$\frac{\mathrm{d}m_\mathrm{r}}{m} = f_\mathrm{r}\frac{\mathrm{d}E_\mathrm{r}}{E}. \tag{8}$$

The values of f_t and f_r can be estimated following analytical arguments or empirical numerical results, as will be elaborated shortly. It is easier to model the mass losses than to model the energy changes, so we proceed by eliminating the energy terms in eq. (6) using the definitions of f_t and f_r.

The mass loss from tidal stripping is computed as

$$\frac{\mathrm{d}m_\mathrm{t}}{m} = -\alpha\xi_\mathrm{t}\frac{\mathrm{d}t}{\tau_\mathrm{dyn}}, \tag{9}$$

where $\xi_\mathrm{t} \equiv [m - m(l_\mathrm{t})]/m$ is the fraction of mass outside the tidal radius, with $m(l_\mathrm{t})$ the mass within the instantaneous tidal radius, l_t; τ_dyn is the dynamical time of the host potential at the GC's instantaneous location, given by

$$\tau_\mathrm{dyn} = \sqrt{\frac{3\pi}{16G\bar{\rho}(r)}}, \tag{10}$$

with $\bar{\rho}(r)$ the average density of the host system within radius r; and $\alpha \approx 0.55$ is an empirical coefficient, calibrated with N-body simulations (Green et al. 2021). The tidal radius is given by (King 1962)

$$l_\mathrm{t} = r\left[\frac{m(l_\mathrm{t})/M(r)}{2 - \mathrm{d}\ln M/\mathrm{d}\ln r + V_\mathrm{t}^2/V_\mathrm{circ}^2(r)}\right]^{1/3}, \tag{11}$$

where $M(r)$ is the host mass within radius r, $V_\mathrm{t} = |\hat{r}\times\boldsymbol{V}|$ is the instantaneous tangential velocity, and $V_\mathrm{circ}(r)$ is the circular velocity.

Similarly, the evaporation caused by two-body relaxation can be expressed as

$$\frac{\mathrm{d}m_\mathrm{r}}{m} = -\xi_\mathrm{e}\frac{\mathrm{d}t}{\tau_\mathrm{r}}, \tag{12}$$

where $\xi_{\rm e} \equiv [m - m(< v_{\rm esc})]/m$ is the fraction of stars in the tail of the velocity distribution that is larger than the escape velocity, which, for an isolated relaxed GC and thus a Maxwellian velocity distribution, is a constant $\xi_{\rm e} \approx 0.0074$; and $\tau_{\rm r}$ is a relaxation timescale, given by (Spitzer 1987; Gieles & Renaud 2016)

$$\tau_{\rm r} \approx 0.142{\rm Gyr}\left(\frac{m}{10^4 M_\odot}\right)\left(\frac{\rho_{1/2}}{10^{11} M_\odot {\rm kpc}^{-3}}\right)^{-1/2}. \quad (13)$$

This is the timescale of refilling the high-speed tail of the velocity distribution.

Combining eqs. (6)-(12), we obtain a unified model for GC structural evolution

$$\frac{{\rm d}\rho_{1/2}}{\rho_{1/2}} = \left[\alpha\left(5 - \frac{3}{f_{\rm t}}\right)\frac{\xi_{\rm t}}{\tau_{\rm dyn}} + \left(5 - \frac{3}{f_{\rm r}}\right)\frac{\xi_{\rm e}}{\tau_{\rm r}}\right]{\rm d}t. \quad (14)$$

The parameters on the right-hand side of eq. (14) all have analytical estimates or empirical values based on numerical simulations.

GR16 adopted $f_{\rm t} = 3$ and $f_{\rm r} = 0$ for the short-term evolution of young star clusters in clumpy interstellar medium; here we estimate $f_{\rm t}$ and $f_{\rm r}$ in the context of the long-term evolution of GCs in a gas-less host. To estimate $f_{\rm t}$, we consider the limit of negligible two-body relaxation, where the GC evolution can be approximated by the tidal evolution of self-gravitating collisionless systems, which has been extensively studied in the context of DM subhalos (e.g., Peñarrubia et al. 2010; Benson & Du 2022). Notably, Peñarrubia et al. (2010) calibrated the tidal evolutionary tracks for DM subhalos using N-body simulations in terms of the maximum circular velocity $v_{\max}$ and the corresponding radius $l_{\max}$ as functions of the bound mass fraction $x = m(t)/m(0)$ and the inner logarithmic density slope $s = -{\rm d}\ln\rho/{\rm d}\ln l|_{l\to 0}$. Turning off two-body relaxation by setting the second term of eq. (14) to zero, i.e.,

$$\frac{{\rm d}\rho_{1/2}}{\rho_{1/2}} = \alpha\left(5 - \frac{3}{f_{\rm t}}\right)\xi_{\rm t}\frac{{\rm d}t}{\tau_{\rm dyn}}, \quad (15)$$

we can therefore find $f_{\rm t}$ by matching the structural evolution according to eq. (15) in terms of $v_{\max}$ and $l_{\max}$ to the tidal track of Peñarrubia et al. for the case of $s = 0$, since young star clusters are generally well described by the Elson et al. (1987) profile and have flat density cores (see Section 2.3). We find that $f_{\rm t}$ is of order unity and mildly decreases with the bound mass fraction:

$$f_{\rm t} = 0.77 x^{0.19},\ x = m/m(0). \quad (16)$$

To estimate $f_{\rm r}$, we follow Gieles et al. (2011) and the seminal work of Hénon (1965) to express the energy change of an isolated GC due to two-body relaxation as

$$\frac{{\rm d}E_{\rm r}}{E} = -\zeta\frac{{\rm d}t}{\tau_{\rm r}}, \quad (17)$$

where $\zeta \approx 0.0926$, assuming equal stellar masses of $0.5M_\odot$ and a Coulomb logarithm of 10 within the star cluster.[2] Comparing eqs. (8), (12), and (17), we obtain

$$f_{\rm r} = \xi_{\rm e}/\zeta \approx 0.08. \quad (18)$$

In summary, for each timestep along the orbit, we evolve the mass of a GC using eqs. (9) and (12), and update the structure of the GC using eq. (14), with the parameters $\alpha = 0.55$, $f_{\rm r} = 0.08$, and $f_{\rm t}$ given by eq. (16). The initial mass and structure of a GC is chosen according to the assumptions that will be given in Section 2.3.

Fig. 3 illustrates the behavior of GCs in the size-mass plane over 10 Gyr according to this model. The GCs are initialized with masses uniformly distributed in logarithmic mass and with sizes according to the median observed size-mass relation of young star clusters (Brown & Gnedin 2021, as will be discussed in Section 2.3). Clearly, the evolution depends on the initial mass. For the most massive GCs ($m \gtrsim 10^6 M_\odot$), the

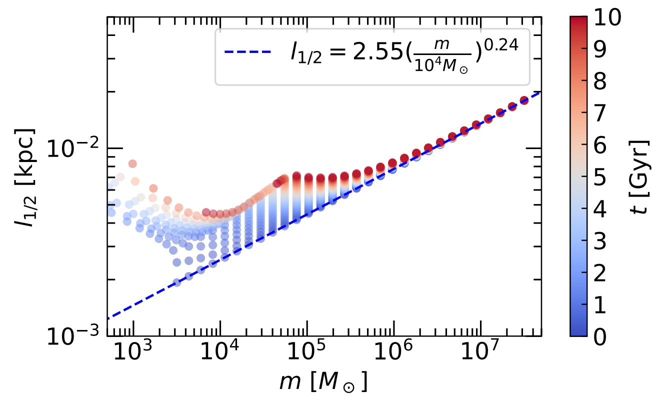

Figure 3. Illustration of the mass-size evolution of star clusters over 10 Gyr according to the model presented in Section 2.2. The star clusters are initialized with masses uniform in $\log m$, sizes following the observed size-mass relation of young star clusters (Brown & Gnedin 2021, blue dashed line), and circular orbits of $r = 5$ kpc in a host potential consisting of an NFW halo with $M_{\rm h} = 10^{12}M_\odot$ and $c = 10$ and a UDG1-like stellar profile. The evolution is mass-dependent, with massive clusters almost intact and low-mass clusters expanding first and then quickly getting tidally truncated and disrupted.

[2] For any realistic stellar mass spectrum, the ζ parameter is larger, up to ~ 0.5 as discussed in GR16.

size and mass barely evolve. For intermediately massive GCs ($m \approx 10^{5-6} M_\odot$), the main effect is expansion due to two-body relaxation, while the mass evolution is marginal. Basically, within 10 Gyr, the expansion barely makes their mass distribution extend to the tidal radius, so there is almost no tidal truncation. For lower-mass clusters ($m \lesssim 10^{4.5} M_\odot$), tidal truncation quickly takes effect as they expand, so they start to lose mass quickly and even dissolve. These mass-dependent behaviors work together to shape the evolved GC mass function in qualitatively the correct direction to that observed, peaking at $m \sim 10^5 M_\odot$. The evolved GC mass distribution would be insensitive to the low-mass end of the initial cluster mass function. With low mass GCs stripped and dissolved, intermediate mass GCs experiencing weak DF, and massive GCs largely intact and thus always experiencing the strongest DF, mass segregation would naturally arise.

2.3. *Model assumptions and GC initialization*

We emphasize that the scenario that this study focuses on is that the observed GC mass-segregation signal is driven by DF and that the strength of it can be used to constrain the DM distribution the host galaxy. Hence, the assumptions are chosen to keep the setup simple and to serve the purpose of testing the constraining power of GC mass segregation on DM halo properties. We assume that the initial cluster mass function (ICMF) follows a power-law with exponential truncations at both the high-mass and low-mass ends (Trujillo-Gomez et al. 2019):

$$\frac{\mathrm{d}N}{\mathrm{d}m} \propto m^{\beta} \exp\left(-\frac{m_{\min}}{m}\right) \exp\left(-\frac{m}{m_{\max}}\right), \tag{19}$$

where $\beta = -2$ reflects hierarchical molecular cloud formation, and $m_{\min}$ and $m_{\max}$ are the lower and upper characteristic scales. We keep $m_{\min} = 10^{5.5} M_\odot$ and $m_{\max} = 10^8 M_\odot$ fixed for simplicity, after having verified that the results are not sensitive to the detailed values as long as they allow for the existence of GCs covering the mass range of $\sim 10^{4.5}$ to $10^6 M_\odot$ [3]. This is partly due to the mass-dependent evolution as shown in Fig. 3, that the low-mass clusters will dissolve in the end.

[3] We emphasize that $m_{\min}$ should not be regarded as the minimum initial mass: because of the functional form of eq. (19) and the power-law slope of $\beta = -2$, with $m_{\min} = 10^{5.5} M_\odot$, the minimum initial star-cluster mass can reach $\sim 10^4 M_\odot$. Similarly, $m_{\max}$ is not the maximum GC mass.

We describe the density profile of a star cluster by an Elson et al. (1987, EFF) functional form,

$$\rho(l) = \frac{\rho_0}{(1 + l^2/a^2)^{\eta}}, \tag{20}$$

where $\rho_0 = \Gamma(\eta) m / [\pi^{3/2} \Gamma(\eta - 1) a^3]$ is the central density, with $\Gamma(x)$ the Gamma function, m the mass of the cluster, -2η the outer logarithmic density slope, and a a scale radius linked to the half-mass radius by

$$a = l_{1/2} / (2^{\frac{2}{2\eta - 3}} - 1)^{1/2}. \tag{21}$$

We adopt $\eta = 2$ such that the outer density slope is -4, motivated by observations of the light profile of young star clusters (Ryon et al. 2015), and assume that the slope is fixed across evolution such that the density-profile evolution is manifested only by the mass and size evolution as in Section 2.2. More analytical properties of the EFF profile can be seen in Appendix B.

With the initial mass drawn from the ICMF, we determine the initial size by sampling from a log-normal distribution based on the observed size-mass relation for young star clusters in the Legacy Extragalactic UV Survey (Brown & Gnedin 2021): the median half-mass radius is given by

$$l_{1/2} = 2.55\,\mathrm{kpc} \left(\frac{m}{10^4 M_\odot}\right)^{0.24}, \tag{22}$$

and the 1σ scatter at fixed mass is approximately 0.25 dex.

We assume that the GC progenitors were all born 10 Gyr ago (Müller et al. 2020; Bar et al. 2022) and that they were isotropically distributed following a Hernquist (1990) profile, $\rho(r) \propto 1/[r(r + r_0)^3]$, with no mass segregation at birth. The initial spatial scale, r_0, of the GC-progenitor spatial distribution is a free parameter to be constrained. We note that the GC-GC merger rate is only $\sim 0.03\,\mathrm{Gyr}^{-1}$ per GC assuming ~ 100 GCs in a dwarf halo of $10^{10} M_\odot$, using the merger criterion in Dutta Chowdhury et al. (2020). We have also numerically verified, using the GC-merger prescription of Modak et al. (2022), that for such a dwarf halo, GC mergers almost all occur at $r \lesssim 0.1\,\mathrm{kpc}$. Hence, to facilitate the MCMC inference, we practically ignore GC-GC encounters and mergers when focusing on the radial mass segregation signal at $r > 0.1\,\mathrm{kpc}$. For the GCs which have lost most of their orbital angular momenta and settle to $r < 0.1\,\mathrm{kpc}$ before getting dissolved, we treat them as merging to form a nuclear star cluster (see Section 4.2).

We treat the host system as a combination of a smooth stellar-mass distribution and a DM halo, both of which remain static during the GC evolution. For the stellar profile, to facilitate orbit integration, we fit a density profile with simple analytical expressions of the gravitational potential to the observed stellar density profile (Bar et al. 2022), given by

$$\rho(r) = \frac{\rho_{0,\star}}{(1+x)\,(1+x^3)} \tag{23}$$

where $x = r/r_{\rm s}$, and $\rho_{0,\star} = 27M_\star/\left[4\pi(9+2\sqrt{3}\pi)r_{\rm s}^3\right]$ with $M_\star = 10^{8.3}M_\odot$ and $r_{\rm s} = 2$ kpc (see Appendix A.3 for more details). For the DM halo, we consider representative functional forms for cuspy and cored profiles, respecitvely – namely, the NFW (Navarro et al. 1997) profile,

$$\rho(r) = \frac{\rho_0}{x\,(1+x)^2}, \tag{24}$$

where $x = cr/r_{\rm vir}$, and $\rho_0 = c^3\Delta\rho_{\rm crit}/[3f(c)]$ with $f(x) = \ln(1+x) - x/(1+x)$; and the Burkert (1995) profile,

$$\rho(r) = \frac{\rho_0}{(1+x)\,(1+x^2)}, \tag{25}$$

where $x = cr/r_{\rm vir}$, and $\rho_0 = M_{\rm h}/\left[2\pi r_{\rm vir}^3 g(c)c^3\right]$ with $g(x) = 0.5\ln(1+x^2) + \ln(1+x) - \arctan x$. It is not obvious whether a core or a cusp is more advantageous for producing the GC mass segregation: for a cored profile, GCs would pile up where the density slope turns flat due to the core-stalling effect, so that the massive GCs that sink to the core radius and the lower-mass GCs that were initially at the core radius are mixed; for a cuspy profile, DF could be so strong that massive GCs sink completely to the center, but leaving the outer GCs not very different in mass. It is therefore interesting to explore which case produces mass segregation more easily and what other differences they may cause.

We initialize the velocities of the star clusters by sampling the velocity distribution function $\mathcal{P}(V|r)$ of a statistically steady-state system in absence of dynamical friction. Specifically, the ergodic energy distribution function is calculated from the Eddington's inversion method (Binney & Tremaine 2008),

$$f(\mathcal{E}) = \frac{1}{\sqrt{8}\pi^2}\left[\frac{1}{\sqrt{\mathcal{E}}}\left(\frac{{\rm d}\rho}{{\rm d}\Psi}\right)_{\Psi=0} + \int_0^{\mathcal{E}}\frac{{\rm d}\Psi}{\sqrt{\mathcal{E}-\Psi}}\frac{{\rm d}^2\rho}{{\rm d}\Psi^2}\right], \tag{26}$$

where $\Psi(r) = -\Phi(r)$. Then the conditional distribution of velocities at each radius r is given by

$$\mathcal{P}(V|r) = 4\pi V^2\frac{f(\Psi(r) - V^2/2)}{\rho(r)}. \tag{27}$$

We draw the speeds from $\mathcal{P}(V|r)$ and assign the directions of the velocity vectors such that they are isotropic in space (e.g., as detailed in Jiang et al. 2021).

2.4. *Paremeter Inference*

We use the affine invariant MCMC ensemble sampler, `emcee` (Foreman-Mackey et al. 2013), to constrain the properties of the host DM halo (i.e. the halo mass $M_{\rm h}$ and the halo concentration parameter c) and the initial scale length of the GC distribution r_0. The observational data that provide the constraints involves the present-day masses of the GCs (m), the half-mass radii ($l_{1/2}$), and the projected distances to the galaxy center (R), from Danieli et al. (2022b). With the primary focus being the radial segregation in mass, we adopt three logarithmic mass bins (as indicated in Fig. 5), and use the median quantities $\langle\log m\rangle_i$, $\langle l_{1/2}\rangle_i$, and $\langle\log R\rangle_i$ for constructing the likelihood. We parameterize the radial mass segregation using two set of quantities: the slopes $\gamma_{ij} \equiv (\langle\log m\rangle_j - \langle\log m\rangle_i)/(\langle\log R\rangle_j - \langle\log R\rangle_i)$, and the number of GCs at each bin relative to the total number of the surviving GCs, f_i. These two quantities measure the steepness of the radial mass segregation and sample the evolved GC mass function, respectively. Overall, we consider a logarithmic likelihood given by

$$\ln(p) = -\frac{1}{2}\sum_k w_k\frac{\left(y_{k,\rm data} - y_{k,\rm model}\right)^2}{y_{k,\rm data}^2}, \tag{28}$$

where $y_{k,\rm data}$ and $y_{k,\rm model}$ refer to the observed values and model predictions, respectively, and y_k represents one of the following quantities, $\{\langle\log m\rangle_i\}$, $\{\langle\log R\rangle_i\}$ $\{\langle l_{1/2}\rangle_i\}$, $\{\langle\gamma\rangle_{ij}\}_{j>i}$, and $\{f_i\}$, with $i, j = 1, 2, 3$ the mass-bin indices, and w_k the weight for the kth quantity. We adopt uniform weighting ($w_k = 1$), which essentially gives the mass-segregation signal an emphasis because there are three γ_{ij} slopes that measure it. We adopt uniform priors for $\log M_{\rm h}$, $\log c$, and the initial spatial scale r_0, within ranges that are chosen according to the galaxy of interest (see Section 3 for example).

To speed up the MCMC inference, instead of evolving the GC populations on the fly for each iteration, we pre-compute the model predictions $y_{k,\rm model}$ on a mesh grid spanned by the parameters of interest. During the MCMC random walk, $y_{k,\rm model}$ is evaluated by linear interpolation. Examples of the pre-computed models can be seen in Appendix C. Note that we opt for not including the total number of GCs as a quantity of interest in our model. This allows us to focus more efficiently on the correlations and on the moments of the observables. Hence, when pre-computing the models, we adopt arbitrarily large initial number of GCs to ensure smooth interpolations. Note that ignoring GC mergers is in-

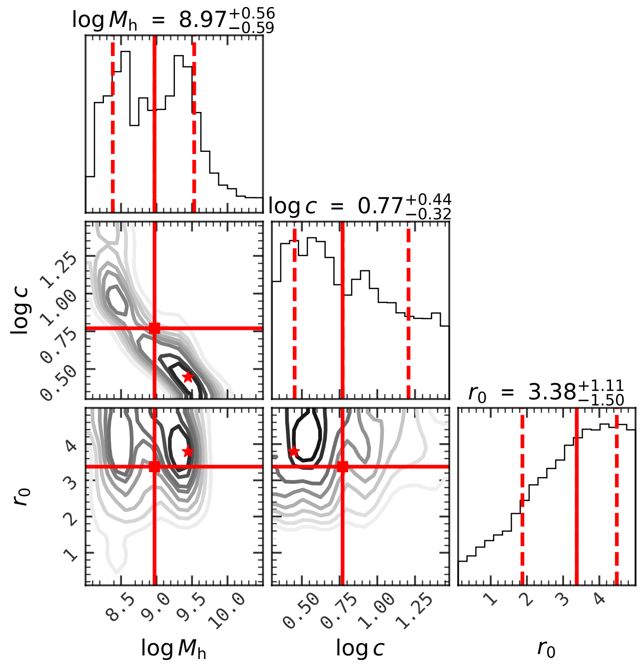

Figure 4. Posterior distributions of the model parameters (halo mass $M_{\rm h}$, halo concentration c, and the scale radius r_0 for the initial star-cluster distribution), assuming an NFW host halo. The red lines indicate the median and the 16th and 84th percentiles. The red stars indicate the 2D projections of the 3D mode value.

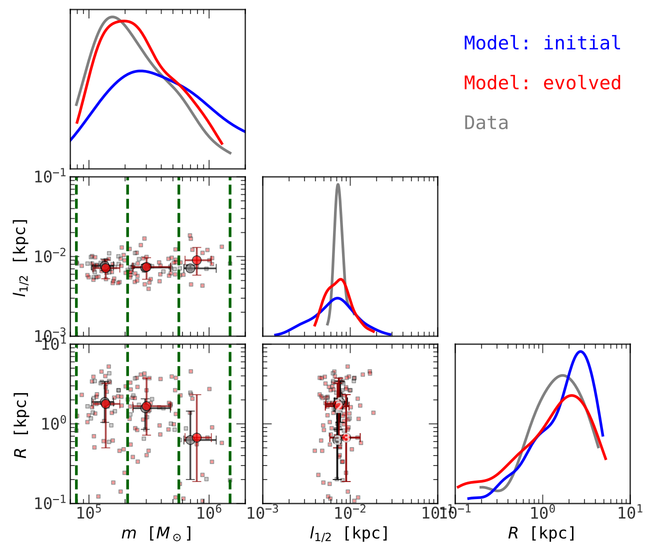

Figure 5. Model realization with an NFW host halo and the mode parameters ($M_{\rm h} = 10^{9.44} M_\odot$, $c = 2.8$, $r_0 = 3.8$ kpc) compared to the data. The diagonal panels show the (individually normalized) one-point functions of star-cluster mass m, size $l_{1/2}$, and galactocentric distnce R. The red circles stand for the median model predictions in the three mass bins (whose boundaries are indicated by the vertical dashed green lines), while the gray circles are those from observation. The error bars indicate the 16th and 84th percentiles. The numbers i shown in the center of the circles in the $R - l_{1/2}$ plane means that this point is for the ith mass bin.

evitable in this approach, since merger rate depends on the total number. That said, when presenting the model realizations corresponding to the posterior models, we adopt an initial GC number that leads to a surviving GC abundance comparable to what is observed.

3. THE DARK-MATTER HALO OF NGC5846-UDG1

As a proof-of-concept, we apply the aforementioned method to study the halo of UDG1 and its GC population. We assume uniform priors of $\log(M_{\rm h}/M_\odot) \in [8, 10.5]$, $\log c \in [\log 2, \log 30]$, and $r_0 \in [0.1, 5]$ kpc, and choose $M_{\rm min} = 10^{5.5} M_\odot$ and $M_{\rm max} = 10^8 M_\odot$ for the ICMF, and evolve the GCs for 10 Gyr, after verifying that the results are not sensitive to slight variations of these values. We use 64 random walkers, and show results of 20000 iterations after 1000 burn-in timesteps. Below, we first present the posterior distributions of the parameters, then compare model realizations with the best-fit parameters with the data, for the two halo-profile scenarios respectively, and finally discuss the results in the context of scaling relations of galaxy-halo connection.

3.1. *NFW halo*

Fig. 4 shows the posterior distributions for NFW host halos. The mode values (in the 3D parameter space) are $M_{\rm h} = 10^{9.44} M_\odot$, $c = 2.8$, and $r_0 = 3.8$ kpc, as indicated by the red stars. The median values, together with the 16th and 84th percentiles, are $\log(M_{\rm h}/M_\odot) = 8.97^{+0.56}_{-0.59}$, $c = 5.9^{+10.3}_{-3.1}$, and $r_0 = 3.4^{+1.1}_{-1.5}$ kpc, as indicated by the red lines. Fig. 5 shows a model realization with the mode parameters.

First, focusing on the R-m plane of Fig. 5, there is a clear trend of mass segregation in the model realization, very similar to that observed. The parameter space that can give rise to such a prominent mass segregation is actually rather limited: a halo significantly more massive than $10^{9.5} M_\odot$ can hardly reproduce the slope and the small distances of the most massive GCs, irrespective of how c or r_0 is varied (see e.g., Appendix C).

Second, the evolved GC size distribution and the size-mass relation are reproduced fairly well: note that the initial GC size distribution is quite broad, but the evolution shrinks the size distribution to better match that observed. Related, the evolved GC size-mass relation is almost flat, as observed, while the initial one has a slope of 0.24. These two trends are largely because the low-mass GCs expand due to two-body relaxation and tidal interactions while the massive ones are almost intact, as discussed in Fig. 3.

Third, the GC mass distribution evolves from an initial broad one towards a narrower distribution in better agreement with what is observed. This is partly because of the depletion of the lowest-mass clusters ($m \lesssim 10^{4.5} M_\odot$), but also partly because some of the most massive clusters ($m \gtrsim 10^6 M_\odot$) have sunk to the center of the system to contribute to the formation of a nuclear star cluster and thus not taken into account here. We will discuss this further in Section 4.

As can be seen from the posteriors in Fig. 4, there is an anti-correlation between halo concentration c and halo mass M_h. This degeneracy is driven by the mass segregation, which can only be achieved with an appropriate amount of DF – overly strong DF would result in orbital decay that is too fast, such that all the massive GCs sink to the center, forming a stellar nucleus instead of a continuous radial mass gradient; overly weak DF would have no effect. Ignoring the Coulomb logarithm, the strength of DF at a radius r can be estimated with the quantity $r\rho(r)/M(r)$, as can be seen from eq. (2), where the DF acceleration a_DF scales linearly with the local density $\rho(r)$ and inversely with the velocity squared, $V^2 \sim GM(r)/r$. For NFW profiles, it is easy to show that this quantity increases with increasing halo mass or concentration, for the radius range of interest ($r \lesssim 5\,\mathrm{kpc}$). This is not the case for a Burkert profile, as will be discussed shortly in Section 3.2.

At the posterior median value, the halo mass of $M_\mathrm{h} \sim 10^9 M_\odot$ corresponds to a $M_\star/M_\mathrm{h}$ ratio of ~ 0.1, much higher than that of normal galaxies. Also interestingly, the concentration is much lower than the cosmological average values. The expected halo concentration is ~ 25 (Dutton & Macciò 2014) for a halo mass of $M_\mathrm{h} \sim 10^9 M_\odot$, $\sim 3\sigma$ higher than the posterior median. We discuss the implications of these findings in Section 3.3.

The initial star-cluster distribution, with a scale distance of $r_0 \sim 3\,\mathrm{kpc}$, is more extended than the present-day smooth stellar distribution of UDG1, which has an effective radius of $2\,\mathrm{kpc}$. This may provide clues for understanding star cluster formation. One scenario is that the star clusters may have formed *ex situ* and been brought in by satellite galaxies, which have since then been disrupted in UDG1 and released their star clusters. The other scenario, perhaps a more natural one given the similar colors of the GCs (Danieli et al. 2022b), is that the clusters may have formed *in situ* but in an extended configuration or with high velocity dispersion, e.g., during collisions of high-redshift gas clouds that belong to different satellite galaxies (Silk 2017; van Dokkum et al. 2022).

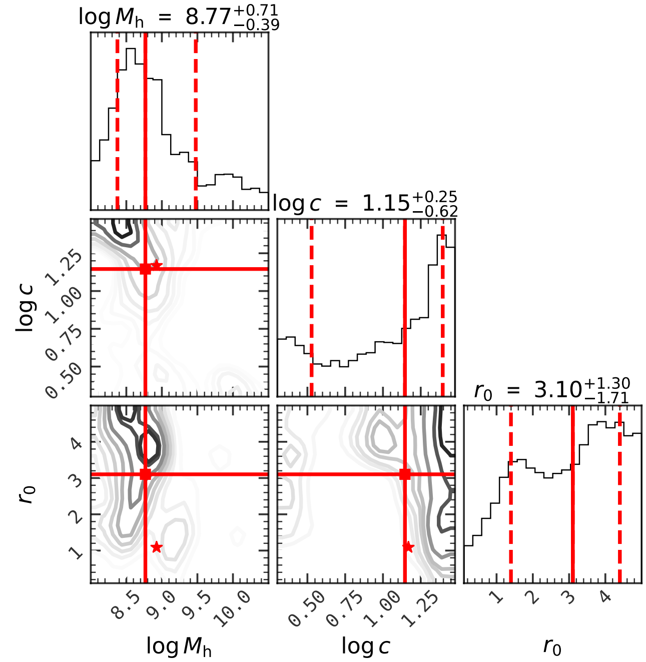

Figure 6. The same as Fig. 4, but assuming a Burkert host halo.

3.2. *Burkert halo*

Fig. 6 shows the posterior distributions with Burkert halos. The results are overall similar to those with an NFW halo, but with subtle, interesting differences. The mode values are $M_\mathrm{h} = 10^{8.93} M_\odot$, $c = 14.8$, and $r_0 = 1.1$ kpc, and the medians with the 16th and 84th percentiles are $\log(M_\mathrm{h}/M_\odot) = 8.77^{+0.71}_{-0.39}$, $c = 14.1^{+11.0}_{-10.7}$, and $r_0 = 3.1^{+1.3}_{-1.7}$ kpc. The halo mass is even lower than that of the NFW case, leaving the galaxy in the DM deficient territory. The concentration is significantly higher than the NFW case, but still smaller than the cosmological expectation for halos of the posterior masses. [4]

For the Burkert halo, the degeneracy between concentration and halo mass is largely absent. Again, this can be understood using the proxy of DF strength, $\rho(r)/V^2_\mathrm{circ}(r)$ – while in the NFW case, increasing c and M_h can both increase this quantity for the radius range of interest ($r \lesssim 5\,\mathrm{kpc}$), it is no longer the case with a Burkert profile. Instead, the $\rho(r)$ change when varying c almost exactly cancels that in V^2_circ. This is also why the constraining power on halo concentration is rather weak. For the initial scale distance r_0, we also obtain a median

[4] Halo concentration usually refers to $c_{-2} = r_\mathrm{vir}/r_{-2}$, with r_{-2} the radius at which the logarithmic density slope is -2. The NFW scale radius r_s is the same as r_{-2}, but the Burkert scale radius $r_\mathrm{s}(= r_\mathrm{vir}/c)$ is $r_{-2}/1.52$, so the Burkert concentration c quoted here is 1.52 times the c_{-2} as commonly reported in cosmological concentration-mass-redshift relations.

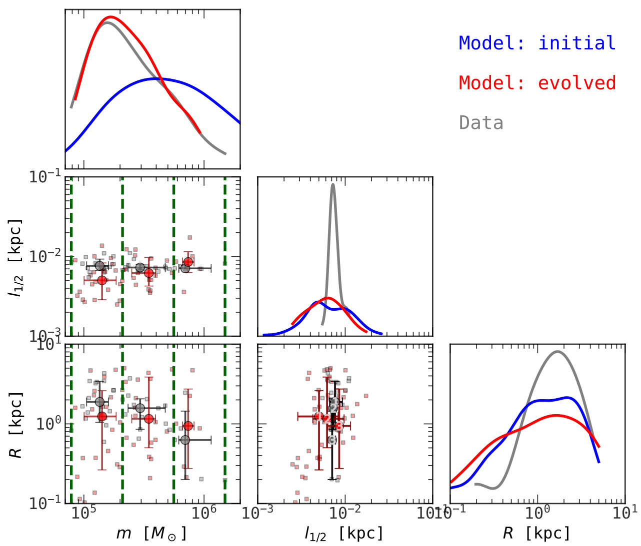

Figure 7. The same as Fig. 5, but for the best-fit Burkert halo ($M_{\rm h} = 10^{8.93} M_\odot$, $c = 14.8$, $r_0 = 1.1\,{\rm kpc}$).

value that is larger than the effective radius of UDG1, so the same formation scenarios could be hypothesized.

Similarly, we generate a model realization of the GC population with the mode parameters of the Burkert halo, and as shown in Fig. 7, it also reproduces most aspects of the data. The segregation trend seems not as strong, but this is partly because of the stochasticity in the random model realization. Hence, either a cuspy halo or a cored halo can more or less reproduce the observed GC statistics. There is a weak but noticeable difference, that intermediate-mass GCs can reach smaller distances in a Burkert host: in the R-m plane, very few model GCs with $m \sim 10^5 M_\odot$ populate the region of $R \lesssim 1\,{\rm kpc}$ in the NFW host, but here there is a more significant low-R tail. The same trend was actually also seen in Bar et al. (2022), which adopted a simpler model and ignored the details of GC evolution. The most obvious difference that the different profile shapes can cause is actually the fraction of GCs that reach the center of the host galaxy and form a nuclear star cluster. We will discuss this further in Section 4.

3.3. *Comparison with scaling relations*

With the aforementioned halo-profile constraints, UDG1 is an outlier in several scaling relations of galaxy-halo connection and halo structure. First, for more massive galaxies, the abundance of GCs, $N_{\rm GC}$, is an excellent indicator of the host virial mass (Harris et al. 2017): a simple linear relation, $M_{\rm vir} = 5 \times 10^9 M_\odot \times N_{\rm GC}$, fits the observational median for almost 5 decades in halo mass from $M_{\rm vir} \sim 10^{10} M_\odot$ to $10^{15} M_\odot$. The scatter of this relation increases towards the lower-mass end, $\sigma_{\log N_{\rm GC}} \propto M_{\rm vir}^{-1/2}$, and is approximately 0.31 dex at

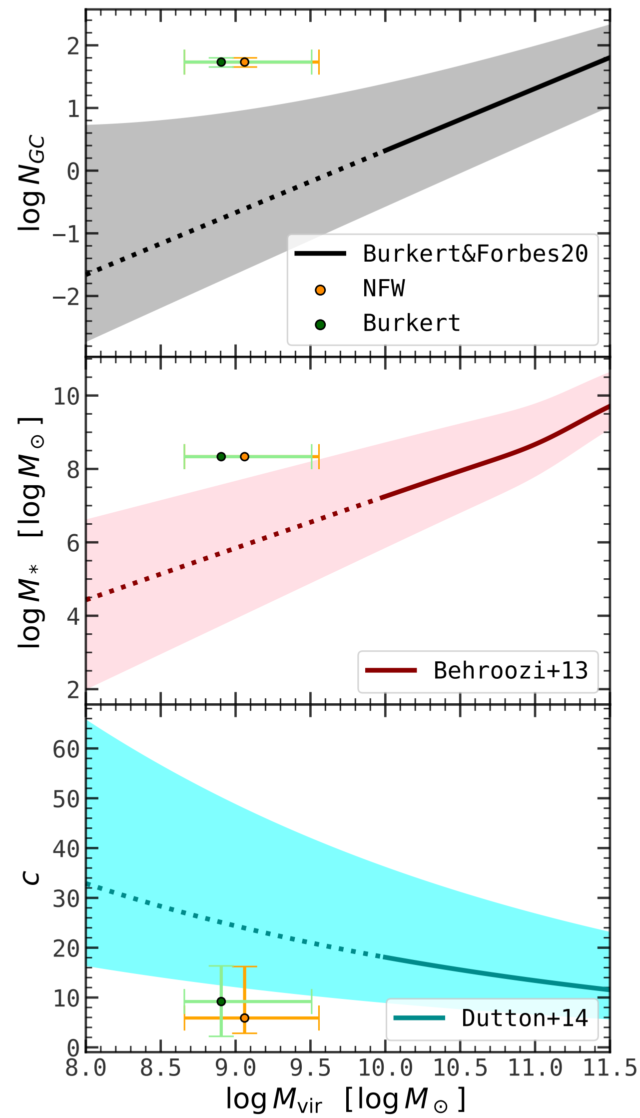

Figure 8. NGC5846-UDG1, with its DM halo constrained with the GC statistics, in comparison with the empirical scaling relations of GC number $N_{\rm GC}$ versus virial mass $M_{\rm vir}$ (*upper*), stellar mass $M_\star$ versus virial mass $M_{\rm vir}$ (*middle*), and halo concentration c versus virial mass $M_{\rm vir}$ (*bottom*). The orange/green circles with error bars represent the medians with the 16th and 84th percentiles, assuming NFW/Burkert halo. The lines stand for the median relations from Burkert & Forbes (2020), Behroozi et al. (2013), and Dutton & Macciò (2014). The dashed parts of the lines indicate extrapolations to a lower mass range than that of the observational or simulation samples from which these relations are extracted. The grey band in the upper panel represents the full scatter of the observational sample as in Burkert & Forbes (2020). The red band in the middle panel indicates the 1σ scatter in $\log M_\star$ at fixed virial mass, as constrained using dwarf satellites in the ELVES sample, from Danieli et al. (2022a). The cyan band indicates the 1σ scatter of 0.3 dex, assuming log-normal distributions of c at fixed virial masses. UDG1 is an outlier to these scaling laws by $\sim 2\!-\!3\sigma$.

$M_{\rm vir} = 10^{11} M_\odot$ (Burkert & Forbes 2020). This relation has been widely used as a halo-mass estimator (e.g., Forbes et al. 2021) and was the basis of the hypothesis that some of the most GC-abundant UDGs are failed L^* galaxies (e.g., van Dokkum et al. 2016). If we assume for simplicity that the scatter in virial mass at a fixed GC abundance is the same as that in the GC abundance at fixed mass, i.e., $\sigma_{\log M_{\rm vir}} = 0.31$ at $N_{\rm GC} = 20$ and $\sigma_{\log M_{\rm vir}} \propto N_{\rm GC}^{-1/2}$, then a galaxy with 50 GCs is expected to have a virial mass of $M_{\rm vir} = 10^{10.7\pm0.2} M_\odot$. Hence, according to our halo-mass estimates, UDG1, with a virial mass of approximately $M_{\rm vir} \sim 10^{9-9.5} M_\odot$, is a dramatic outlier to this empirical $N_{\rm GC}$-$M_{\rm vir}$ relation (as extrapolated to the lower mass range) by several σ. We illustrate this in the upper panel of Fig. 8. Here, the grey band actually represents the full width of the distribution of the observational sample compiled by Burkert & Forbes (2020) – despite the increase of the scatter at the low-mass end, UDG1 is still an outlier.

However, the $N_{\rm GC}$-$M_{\rm vir}$ relation is based on massive galaxies, so the extrapolation to the low-mass end ($M_{\rm vir} \gtrsim 10^{10} M_\odot$) is ungrounded, and the scatter of the relation may contain systematics with morphology. In fact, as Burkert & Forbes already noticed, in their effort of explaining this relation with halo merger trees, the relation must flatten at $M_{\rm vir} \lesssim 10^{10} M_\odot$ or $N_{\rm GC} \lesssim 100$, which is exactly the regime of GC-rich UDGs. This flattenning is supported by the observational sample of dwarf galaxies whose virial masses are individually constrained with gas kinematics Forbes et al. (2018), as represented by the grey band in Fig. 8. Our virial-mass estimate of UDG1 is qualitatively in line with the flattening of the $N_{\rm GC}$-$M_{\rm vir}$ relation at the low-mass end, but more extreme, highlighting the danger of naively inverting the relation to infer virial mass with the number of GCs.

Second, UDG1 is an outlier to the stellar-mass-total-mass relation from abundance matching, as illustrated in the middle panel of Fig. 8. For comparison, we have chosen the median relation as in Behroozi et al. (2013), and recent estimate of the low-mass-end scatter using the dwarf satellites in the ELVES sample Danieli et al. (2022a). We caution that despite being intensively studied, the low-mass end of the relation remains highly uncertain, and different assumptions lead to different results (see e.g., Danieli et al. 2022a, and the references therein). Our particular choice here is among the most flat for the low-mass-end median slope and among the largest in the scatter – even with these conservative choices, UDG1 is a $\sim 2\sigma$ outlier.

Third, as the bottom panel of Fig. 8 shows, UDG1 stands out with respect to the concentration-mass relation of DM halos. For comparison, we have shown a median c-$M_{\rm vir}$ relation from cosmological N-body simulations (Dutton & Macciò 2014), with a constant scatter of 0.3 dex assuming log-normal c distribution at fixed $M_{\rm vir}$ (Diemer & Kravtsov 2015; Benson 2020).[5] Obviously, the UDG1 halo is less concentrated than what is expected cosmologically for its mass. This is consistent with the scenario that UDG formation results from repeated supernovae feedback, which makes both the halo less concentrated and also the stellar distribution puffy (e.g., Jiang et al. 2019; Freundlich et al. 2020).

In short, the UDG1 DM halo stands out as a $\sim$2-3σ outlier compared to all the aforementioned scaling relations, irrespective of the assumed density-profile shape. It is in line with the understanding that there is huge scatter in these relations at the low-mass end, and warns us against generalizing these relations to extreme galaxies and using them as virial mass estimators. We caution that our halo mass estimates for UDG1 is based on the assumption of a static host halo, whereas in reality the UDG1 halo might be a satellite of the galaxy group NGC5846, and thus have been environmentally processed. It may also have internally-driven evolution due to supernovae feedback. To consider the host halo of UDG1 as a subhalo evolving in mass and structure is beyond the scope of this work, but it is reasonable to speculate that the peak virial mass of the system in the past is higher than our estimates here, and thus brings the system closer to the empirical scaling laws.

4. DISCUSSION

In this section, we first discuss a few observational implications, including the line-of-sight (LOS) velocity dispersion of the GCs in UDG1, and the fraction of nuclear star clusters. Second, we compare our model with that of the previous work of Bar et al. (2022) and Modak et al. (2022). Finally, we comment on the simplifications in this work, and point out potential future improvements and applications of our method.

4.1. *Velocity dispersion of the GCs*

In Fig. 9, we present the LOS velocity-dispersion profile of the evolved GCs in halos of the best-fit parameters. The dispersion profiles in the Burkert halo and in the NFW halo are similar, and, in comparison with that of smooth stars, which reflect the equilibrium kinematics of the host potential, both show a significant decrease, more so at smaller R. This is another manifesta-

[5] The scatter in principle varies with mass and the selection of halos based on whether they are relaxed, and 0.3 dex is a ballpark estimate.

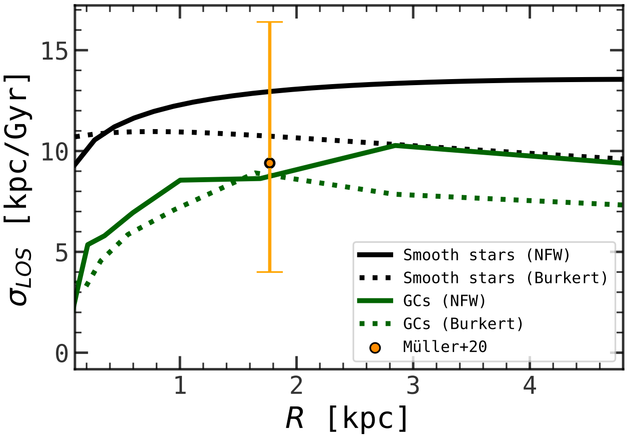

Figure 9. LOS velocity-dispersion profiles of the GC population in comparison with that of the smooth stars. The lines represent our best-fit model results of, the smooth stars in the best-fit NFW halo (black solid), the smooth stars in the best-fit Burkert halo (black dotted), the evolved GCs in the NFW halo (green solid), and the evolved GCs in the Burkert halo (green dotted). The orange circle with error bar is inferred from the observed kinematics, based on about one fifth of all the ~ 50 member GCs (Müller et al. 2020).

tion of DF, besides mass segregation. Observationally, Müller et al. (2020) have measured the velocities of 11 of the member GCs of UDG1, and inferred a dispersion of $\sigma = 9.4^{+7.0}_{-5.4}$ km/s at $R \approx 1.8$ kpc (i.e., the average distance of the 11 GCs to the galaxy center), assuming a simple pressure-supported spherical system. Our model predictions agree with this measurement. In fact, a closer examination of the posterior distribution of the GC velocity dispersion of Müller et al. (2020) reveals that the mode value is approximately 8 km/s, almost exactly on top of our model results.

Interestingly however, Forbes et al. (2021) measured the velocities of the smooth stellar distribution of UDG1 using KCWI on the Keck telescope, and found a rather high value of the smooth-star velocity dispersion of $\sigma_\star = 17 \pm 2$ km/s, higher than the equilibrium value ($\sigma \sim 13$ km/s) of a low-mass ($M_{\rm vir} \sim 10^9 M_\odot$) system as advocated here, and more consistent with a virial mass of $M_{\rm vir} \sim 10^{9.5-10} M_\odot$. We opt not to dive into the factors that may reconcile the 2σ tension, such as oversimplifications in our model or non-equilibrium of the stellar distribution. Instead, we can see that these two observational studies together (Müller et al. 2020; Forbes et al. 2021) present a qualitatively similar picture as what our model reveals here, i.e., the GCs of UDG1 have smaller velocity dispersion than the smooth stars, indicative of DF, and the virial mass of UDG1 is lower than what is expected from the scaling laws.

4.2. *Nucleated ultra-diffuse galaxies*

A significant fraction of UDGs are nucleated, in the sense that they feature a compact stellar distribution at or near the geometric center of the system (Lim et al. 2018; Greco et al. 2018; Iodice et al. 2020; Marleau et al. 2021). The compact stellar source, also known as the nuclear star cluster (NSC), is more compact than a stellar bulge as in an early-type galaxy and is more massive than a typical GC – imaging samples can be found at Lim et al. (2018, Fig.3). The fraction of UDGs that are nucleated is approximately 30-40% in nearby galaxy clusters, and seem to show an environment dependence such that the fraction is higher in the densest region and decreases towards the outskirts of the galaxy cluster (Lim et al. 2018).

It it natural to attribute the formation of an NSC to the coalescence of the GCs which have lost their orbital angular momentum completely due to DF and sunk to the center. If this is the case, we can expect that different DM profiles, as well as different initial GC distributions, can determine the nucleatedness of a UDG and the mass of the NSC. Modak et al. (2022) already showed that NSCs only form in cuspy halos and almost never form in a cored halo. Here we revisit this scenario using our model, which is more refined in terms of GC evolution compared to the previous work. We emphasize that this experiment is for GC-rich dwarfs in general, no longer aimed at reproducing UDG1. We quantify the nucleatedness of the resulting system using the mass fraction of the nucleus, $f_{\rm nucleus}$, defined as the total mass of the GCs that settle to $r < 0.1$ kpc, divided by the total mass of all the GCs.

Fig. 10 shows $f_{\rm nucleus}$ as a function of halo mass $M_{\rm h}$, halo concentration c, and the initial Hernquist scale of the GC distribution r_0. Here, a cuspy NFW profile and a cored Burkert profile exhibit a dramatic difference, in the sense that the nucleus fraction in a cored halo is almost zero (except for the combination of the lowest $M_{\rm h}$, highest c, and largest r_0), whereas that of a cuspy halo is significant, as long as the halo mass is below $M_{\rm h} \sim 10^{10} M_\odot$. The negligible nucleus fractions of a cored halo is due to the stalling effect, which prevents the GCs from dropping deeper (see Banik & van den Bosch 2022, for a thorough discussion) and is empirically captured by the Petts et al. (2015) prescription adopted here.

There are trends of the nucleus fraction with the model parameters. First, larger halo mass leads to smaller $f_{\rm nucleus}$. This is because of the dependence of the DF strength on the mass ratio between the GC and the host. Second and intuitively, larger scale length leads to smaller $f_{\rm nucleus}$, since if GCs start out at large dis-

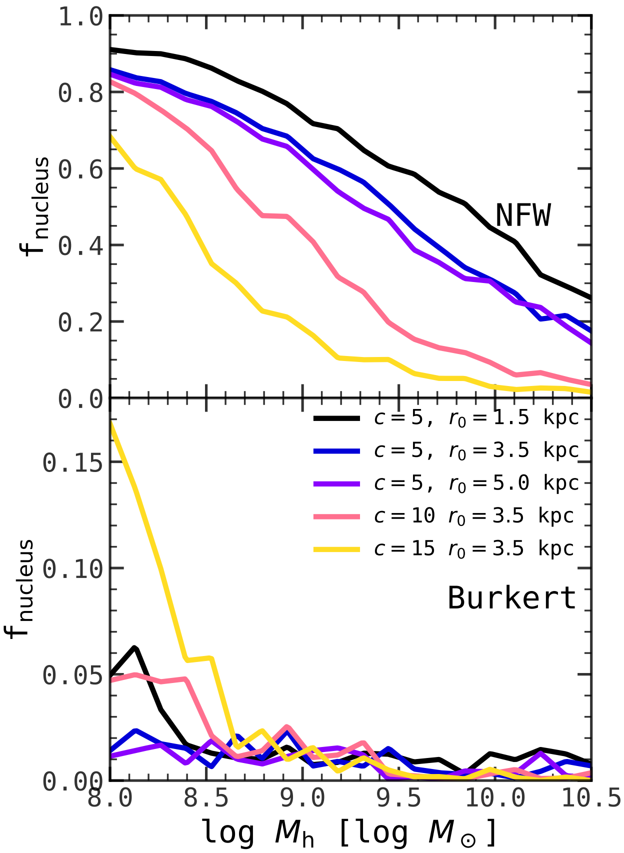

Figure 10. The mass fraction of nuclear star cluster (the total mass of the GCs that have sunk to the center of the galaxy due to dynamical friction, divided by the total mass of all the GCs in the galaxy) as a function of halo mass. The upper and lower panels show the results assuming cuspy (NFW) and cored (Burkert) profiles, respectively. Different colors represent different combinations of the halo concentrations (c) and the scale length (r_0) of the initial GC distribution, as indicated. Clearly, a cuspy, low-mass halo easily gives rise to nucleated systems, while the cored profile yields negligible nuclear star cluster for most parameter combinations.

tances, they need stronger DF or longer time to sink to the center. Third, as to the concentration dependence, for NFW halos, a higher concentration leads to a lower $f_{\rm nucleus}$, at fixed halo mass. This, again, can be attributed to the competing effects on DF from c and $M_{\rm h}$, as we discussed in the context of the c-$M_{\rm h}$ degeneracy of a cuspy halo in Section 3.1. For Burkert halos, the c-trend is vague, and can similarly be attributed to the null effect of varying c on the DF acceleration as we argued in Section 3.2. The difference in the nucleus fraction between the cuspy and cored cases implies the possibility of using NSCs to infer the DM distribution of UDGs, and could be further explored in future statistical studies.

4.3. *Comparison with previous studies*

Bar et al. (2022) also studied the mass segregation of GCs in UDG1 using a semi-analytical model of similar nature to ours. Modak et al. (2022) studied GC statistics in a more compact dwarf galaxy but adopted a very similar model to that of Bar et al.. There are a couple of major improvements here in our approach.

First, the previous studies did not trace the mass and structural evolution of GCs along the orbits, but instead adopted, e.g., as in Bar et al., a simple empirical model of GC mass loss, $m(t) = m(0)\,(1-\delta t/t_0)$ with $\delta = 0.3$, $t_0 = 10$ Gyr, for all the GCs. That is, the mass evolution is linear with time, irrespective of the local tidal field, and there is no structural evolution. Modak et al. makes the mass evolution exponential, but the other aspects remain the same. Related, the GC mass distribution in these works were manually set to match that observed. As discussed in Section 2, the mass and structural evolution affects the DF strength, via the Coulomb logarithm, and thus the orbit evolution could be different if the mass or size is not properly accounted for. In our model, the GCs evolve self-consistently in mass and structure under the influence of tidal effects and two-body relaxation. Besides, the evolution starts from theoretically-motivated or observationally-motivated initial mass functions and initial structural distributions. As such, besides the GC mass segregation signal, the evolved GC mass function and size-mass relation are also emergent predictions in our model, and, as demonstrated, they both agree decently with the data.

Second, the previous studies did not aim at statistically constraining the DM halo mass or structure. Instead, they adopted a couple of somewhat arbitrary fixed halo masses and profiles, and tested whether mass segregation could arise under these somewhat arbitrary choices. For example, Bar et al. used an NFW host with $M_{\rm h} = 10^{9.78}M_\odot$ and $c = 6$ and a Burkert host with $M_{\rm h} = 10^{9.53}M_\odot$ and $c = 15.4$. Basically, their halo masses are approximately an order of magnitude higher than what we found here, and their halo concentrations happen to be in the same ballpark with our posterior mode values. Interestingly however, they could achieve mass segregation with these more massive halos, whereas our model cannot.

The main factor that causes the difference lies in the star-cluster evolution – with our model, mass loss depends on the instantaneous internal and external conditions, such that the clusters getting closer to the host center experience stronger mass loss. This counterbalances the mass-segregation effect of DF. Hence, to obtain mass segregation with our model, stronger DF is

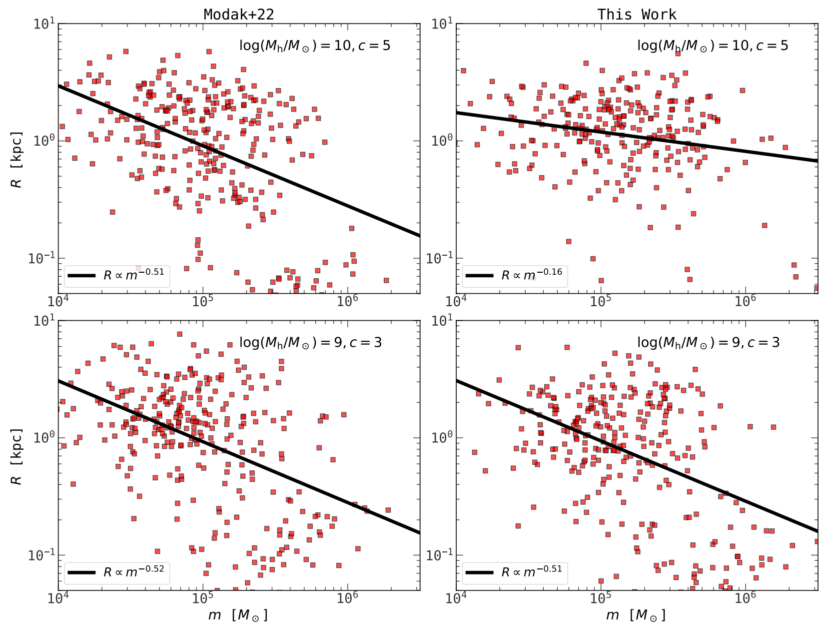

Figure 11. Illustration of the impact of the star-cluster evolution model on the halo mass at which GC mass segregation occurs: projected galacto-centric distance versus GC mass, in host halos of given mass and concentration, as quoted, obtained using the Modak et al. (2022) model (*left*) and the model presented in this work (*right*) with the same initialization scheme. To make the results statistically robust, 20 random realizations of 50 initial star clusters are included. Linear regression results are overplotted to gauge the strength of the mass segregation. *Upper panels:* with a relateively massive halo ($M_{\rm h} = 10^{10} M_\odot$), our model produces marginal mass segregation, while the Modak et al. model, featuring orbit-independent mass loss and neglecting star-cluster size in the dynamical-friction treatment, can already produce fairly strong mass segregation. *Lower panels:* with a lower halo mass of $M_{\rm h} \sim 10^9 M_\odot$ and a low concentration, both models can produce mass segregation.

needed, which translates to a lower halo mass because of the dependence of DF on the perturber-to-host mass ratio. This is illustrated in Fig. 11, where we keep the host halo as well as the initialization of coordinates and velocities the same, and evolve the star clusters using the Modak et al. model and our model, respectively, for results shown in the left and right panels. The mass initialization cannot be exactly the same because of the difference in the evolution prescriptions, but we have adjusted the ICMF to make the evolved mass distributions comparable. As can be seen, with the Modak et al. model, significant mass segregation can already be produced for a relatively massive NFW host halo of $M_{\rm h} = 10^{10} M_\odot$, while our model produces a marginal trend for this mass. For the lower halo mass of $M_{\rm h} = 10^9 M_\odot$, both models can produce similarly strong mass segregation.

Another factor here is that the previous studies did not follow star-cluster structural evolution. As we already discussed, neglecting size results in a larger Coulomb logarithm and thus stronger DF. In short, it is easier to get mass segregation with the Modak et al. and Bar et al. models, because the mass loss is orbit-independent and because DF is stronger when neglecting the cluster size. It is therefore important to model GC evolution accurately for the purpose of constraining DM distribution.

4.4. *Simplifications and future work*

While in this work we have improved upon previous studies by introducing a self-consistent physical model of GC evolution and employing MCMC to constraint the DM halo properties, we caution that there are still over-simplifications that leave room for future improvements. Addressing them quantitatively is beyond the scope of current work, but here we point out qualitatively how they might affect the results and sketch ideas for future studies. The discussion applies not just to the specific galaxy UDG1, but to GC-rich dwarf galaxies in general.

First, we have assumed that the host potential is static over the entire evolution of the GC population. However, UDG1 is a satellite galaxy of the galaxy group NGC5846, and many GC-rich low-surface-brightness galaxies are members of galaxy groups or clusters. That is, the host halo of UDG1 may be a subhalo that has experienced significant mass loss if it had orbital pericenters sufficiently close to the center of the host group. In the case, UDG1 may lie closer to the scaling relations (Section 3.3) if its peak virial mass and the concentration at the peak mass are used in place of the present-day values. In fact, it has been argued that the differential tidal mass loss between the subhalo and the stellar component can produce DM-deficient dwarf galaxies (Moreno et al. 2022). Even for an isolated dwarf galaxy, the host halo is not static, but increases in mass gradually. It is in principle possible to parameterize the mass assembly history of the host halo or subhalo using empirical models extracted from cosmological simulations (e.g., Wechsler et al. 2002). However, this would introduce additional model parameters that need to be marginalized over, not to mention that there is significant halo-to-halo variance in the mass histories (Jiang & van den Bosch 2017) so that a certain choice of the parameterization may not be representative. A more viable way of exploring statistically the effect of a dynamic host is to post-process cosmological numerical or semi-ananlytical simulations and populate simulated halos with GCs and study the GC statistics. We leave this idea to a future study.

Second, there are a few other mechanisms for GC mass and structural evolution besides tidal interactions and two-body relaxation, including, among others, stellar evolution and gravothermal core-collapse. Lamers et al. (2010) provide an empirical formula for mass loss of GCs due to stellar evolution obtained from collisional N-body simulations. Following their model, GCs lose $\sim 25\%$ of their initial mass over 10 Gyr, insensitive to their initial masses. Therefore, this effect can simply be offset by shifting the ICMF. The more complicated effect is the gravothermal core-collapse of GCs, which steps in after when an isothermal core is established due to two-body relaxation. The core contracts since it is dynamically hotter than the outer part and transports energy to the outskirts. This makes the GC profile deviate from the EFF profile assumed in this work (or more generally, the King models), and become cuspy and resistent to tidal mass loss. The core-collapse timescale has been estimated to be 12-19 times the relaxation time $\tau_{\rm r}$ given in eq. (13) (Quinlan 1996), so it can be shorter than the Hubble time for the lower mass GCs ($m \lesssim 10^{4.5} M_\odot$).

Third, if future kinematics observations can narrow down the DM profile, we can then adapt our model to constrain the other model ingredients. For instance, while the ICMF is believed to follow the functional form of eq. (19), the power-law slope as well as the mass scales are not fully constrained and likely exhibit variation from one population to another (see e.g., Alexander & Gieles 2013, for a discussion on the power-law slope). It would be interesting to treat the ICMF parameters as free parameters, and combine the GC evolution model and the MCMC method as in this study to constrain the ICMF, to investigate, for example, whether UDGs have a unique ICMF.

5. CONCLUSION

In this work, we are motivated by a remarkable ultra-diffuse galaxy, NGC5846-UDG1, whose globular-cluster population exhibits interesting radial mass segregation, and aim to explore the possibility of reproducing the mass segregation of the GCs with dynamical friction and constraining the dark-matter content of the UDG using photometric data alone. To this end, we have introduced a simple semi-analytical model that describes the evolution of GC populations in their host DM halo and galaxy, accounting for the effects of DF, tidal evolution, and two-body relaxation. We also consider educated assumptions of the initial properties of the GC progenitors, including the mass function, structure, and spatial distributions. We forward model the GCs in a UDG1-like host potential (consisting of a DM halo and a smooth stellar distribution) to match the observed GC statisitcs from Danieli et al. (2022b), and use MCMC to constrain the DM distribution (halo mass $M_{\rm h}$ and concentration c) of UDG1, as well as the scale radius of the initial star-cluster spatial distribution (r_0). While we have focused on UDG1, the methodology developed here is generally applicable to dwarf galaxies with a rich GC population. We summarize our methodology and the main findings as follows.

We have shown that the orbital evolution under the influence of DF depends on the mass and structural evolution. Our model can self-consistently evolve the mass and structure of individual GCs along their orbits, capturing the effect of a varying tidal field along an eccentric orbit around the central region of a galaxy. In the limit of a weak tidal field, the mass and structural evolution in our model reduces to that of the classical work of Hénon (1965); while in the limit when the timescale for tidal stripping is shorter than two-body relaxation, the structural evolution follows that of the empirical tidal evolution track for collisionless systems of Peñarrubia et al. (2010) with cored density profiles, which applies to the assumed EFF density profiles of the GCs. Reassuringly, over the timescale of $\sim$ 10 Gyr, a population of star clusters drawn from reasonable initial cluster mass functions (Trujillo-Gomez et al. 2019) and initial structure-mass distributions (Brown & Gnedin 2021) evolves in a converging manner regarding its evolved mass and size distributions – notably, the lower-mass clusters ($m \lesssim 10^{4.5} M_\odot$) expand and get dissolved more easily, whereas the most massive clusters ($m \gtrsim 10^6 M_\odot$) remain largely intact, making the evolved GC mass function peak at $m \sim 10^5 M_\odot$ and the evolved GC size-mass relation flat, as observed.

No matter whether the density profile of UDG1 is cuspy or cored, we find that the DM halos that can give rise to the observed mass segregation are of low mass and low concentration. In particular, with an NFW (Burkert) halo, we obtained a posterior-mode halo mass of $M_{\rm h} = 10^{9.44} M_\odot$ ($10^{8.93} M_\odot$) and concentration of $c_{-2} = 2.8$ (9.7). There is a concentration-mass degeneracy (anti-correlation) in the case of an NFW profile, driven by the similar effects of increasing concentration and increasing mass on the DF strength in the central few kpc of the host potential. Given the stellar mass of UDG1 of $M_\star \sim 10^8 M_\odot$, these halo-mass estimates put UDG1 in the DM-deficient territory.

In fact, UDG1 is a dramatic outlier compared to both the stellar-to-total-mass relation (e.g., Behroozi et al. 2013; Danieli et al. 2022a) and the GC-abundance-total-mass relation (e.g., Harris et al. 2017; Burkert & Forbes 2020). The latter relation is known to flatten and increase in scatter at the low-mass end, and UDG1, with our halo-mass estimates, is in qualitative agreement with this trend, though more extreme. This warns against using this relation naively for halo-mass estimates for UDGs.

The estimated halo concentrations are lower than the cosmological average value expected for halos of the posterior masses. This lends support to the theoretical picture that UDGs populate low-concentration halos, which are puffed up by repeated supernovae outflows or environmental effects (e.g., Di Cintio et al. 2017; Chan 2019; Jiang et al. 2019). The posterior scale distance of the initial star-cluster distribution (which is assumed to follow an Hernquist profile) is $r_0 \sim 3\,$kpc. Hence, the star clusters were likely in a more extended configuration initially than the (present-day) smooth stars which has an effective radius of 2 kpc. This may imply that the star clusters are either of *ex-situ* origin or formed *in situ* but in an extended configuration achievable via collisions of high-redshift gas clouds.

The radial mass segregation of GCs can be reproduced with either assumption of the halo profile, if we just focus on the distance-mass slope of the GCs that have not sunk to the center of the galaxy (Section 3). However, if we include all the GCs including the ones that have completely lost orbital angular momentum due to DF, and consider the nuclear star cluster that form out of GC mergers at the center of the galaxy, then the cuspy NFW halo can yield massive nuclear star clusters provided that the halo mass is below $10^{10} M_\odot$, whereas cored halos do not result in any significant nuclear star cluster. Therefore, a viable formation mechanism for nucleated UDGs (e.g. Lim et al. 2018) is the orbital decay of GCs in a low-mass cuspy halo (see also Modak et al. 2022). As UDG1 seems to be a non-nucleated UDG, our results suggest that it is more likely to be hosted by an cored, low-mass DM halo. This is, again, in line with the theoretical picture that UDG formation goes hand-in-hand with the core formation of DM halos due to non-adiabatic perturbations of the gravitational potential.

Last but not the least, compared to the observationally-costly kinematics measurements, our model can reproduce the observed LOS velocity dispersion of the GCs (Müller et al. 2020), and can reveal the difference between the velocity dispersion of the GCs and the smooth stellar background. This also manifests DF and is in qualitative agreement with what is observed (Forbes et al. 2021).

In summary, we have demonstrated with the case study of UDG1 that, as long as dwarf galaxies host a statistically significant number of GCs and the GCs form a radial mass trend, one can use a computationally efficient semi-analytical model such as the one laid out in this work to constrain the hosting DM distributions. This is in principle feasible with imaging data alone. However, getting clean samples of GCs with little contamination from background galaxies or foreground stars requires deep, high-resolution imaging – this will soon be enabled by upcoming instruments, such as the Vera C. Rubin Observatory (LSST), the Chinese Survey Space Telescope (CSST), and Nancy Grace Roman Space Telescope (WFIRST).

FJ thank Avishai Dekel, Aaron Romanowski, Frank van den Bosch, Hui Li, Kyle Kremer, Xiaolong Du, Ethan Nadler, and Jacob Shen for helpful general discussions. JL acknowledges the Tsinghua Astrophysics High-Performance Computing platform at Tsinghua University for providing computational resources for this work.

Software: `EMCEE` (Foreman-Mackey et al. 2013), `SatGen` (Jiang et al. 2021)

APPENDIX

A. ANALYTICS OF STELLAR PROFILES AND DM HALO PROFILES

This section presents useful analytical expressions for the profiles we use in this work, including NFW (Navarro et al. 1997), Burkert (Burkert 1995), and a profile that describes the stellar density of NGC5846-UDG1. The density profiles are already given in the main text, here we list the enclosed mass (M), gravitational potential (Φ), gravitational acceleration in the cylindrical coordinate system (f_R, $f_\phi = 0$, f_z), and the one-dimensional velocity dispersion (σ) for an isotropic velocity distribution are presented.

A.1. *NFW*

$$M(r) = M_{\rm h}\frac{f(x)}{f(c)}, \tag{A1}$$

where $x = r/r_{\rm s}$ and $f(x) = \ln(1+x) - x/(1+x)$.

$$\Phi(r) = \Phi_0\frac{\ln(1+x)}{x}, \tag{A2}$$

where $\Phi_0 = -4\pi G\rho_0 r_{\rm s}^2$

$$f_R = -\frac{\partial\Phi}{\partial R} = \Phi_0\frac{f(x)}{x}\frac{R}{r^2}\ \ , f_z = -\frac{\partial\Phi}{\partial z} = \Phi_0\frac{f(x)}{x}\frac{z}{r^2}, \tag{A3}$$

where $r = \sqrt{R^2+z^2}$.

$$\begin{aligned}\sigma^2(r) &= -\Phi_0 x(1+x)^2\int_x^\infty \frac{f(x')}{x'^3(1+x')^2}{\rm d}x' \\ &\approx V_{\rm max}^2\left(\frac{1.439x^{0.354}}{1+1.176x^{0.725}}\right)^2\end{aligned} \tag{A4}$$

where the second line is an approximation accurate to 1% for $x = 0.01$-100 (Zentner & Bullock 2003).

A.2. *Burkert*

$$M(r) = 2\pi\rho_0 r_{\rm s}^3 g(x), \tag{A5}$$

where $\rho_0 = M_{\rm h}/\left[2\pi r_{\rm vir}^3 g(c)c^3\right]$, $g(x) = 0.5\ln(1+x^2) + \ln(1+x) - \arctan x$, and $x = r/r_{\rm s}$.

$$\begin{aligned}\Phi(r) = \frac{\Phi_0}{4x}\Big\{&2\left(1+x\right)\left[\arctan\frac{1}{x} + \ln\left(1+x\right)\right] \\ &+ \left(1-x\right)\ln\left(1+x^2\right) - \pi\Big\},\end{aligned} \tag{A6}$$

where $\Phi_0 = -4\pi G\rho_0 r_{\rm s}^2$.

$$f_R = -\frac{\partial\Phi}{\partial R} = \Phi_0\frac{f_0}{x^2}\frac{R}{r_{\rm s}}\ \ , f_z = -\frac{\partial\Phi}{\partial z} = \Phi_0\frac{f_0}{x^2}\frac{z}{r_{\rm s}}, \tag{A7}$$

where $r = \sqrt{R^2+z^2}$ and $f_0 = 2\arctan\frac{1}{x} + 2f(x) + 2\arctan x - \pi$.

$$\begin{aligned}\sigma^2(r) &= -\frac{\Phi_0}{2}\left(1+x\right)\left(1+x^2\right)\int_x^\infty \frac{f(x')}{x'^2(1+x')(1+x'^2)}{\rm d}x' \\ &\approx V_{\rm max}^{0.299}\frac{e^{x^{0.17}}}{1+0.286x^{0.797}}.\end{aligned} \tag{A8}$$

A.3. *UDG1 stellar profile*

$$\begin{aligned}M(r) = \frac{M_\star}{2(9+2\sqrt{3}\pi)}&\Big[\sqrt{3}\pi + 18f_3(x) \\ &-6\sqrt{3}f_2(x) + 9f_3(x)\Big],\end{aligned} \tag{A9}$$

where $x = r/r_{\rm s}$ with $r_{\rm s}$ a scale radius ($r_{\rm s} = 2\,{\rm kpc}$); and

$$f_1(x) = \ln\frac{1-x+x^2}{(1+x)^2}, \tag{A10}$$

$$f_2(x) = \arctan\frac{1-2x}{\sqrt{3}}, \tag{A11}$$

$$f_3(x) = \frac{x}{1+x}. \tag{A12}$$

$$\begin{aligned}\Phi(r) = \frac{\sqrt{3}\Phi_0}{54x}&\big[(1+6x)\pi \\ &+6(2x-1)f_2(x) + 3\sqrt{3}f_1(x)\big],\end{aligned} \tag{A13}$$

where $\Phi_0 = -4\pi G\rho_0 r_{\rm s}^2$.

$$f_R = -\frac{\partial\Phi}{\partial R} = \frac{\Phi_0 C}{54r^2}\frac{R}{x}\ \ , f_z = -\frac{\partial\Phi}{\partial z} = \frac{\Phi_0 C}{54r^2}\frac{z}{x}, \tag{A14}$$

where $C = \sqrt{3}\pi + 18f_3(x) - 6\sqrt{3}f_2(x) + 9f_1(x)$.

$$\begin{aligned}\sigma^2(r) &= -\frac{\Phi_0}{54}\left(1+x\right)\left(1+x^3\right) \\ &\times\int_x^\infty \frac{\sqrt{3}\pi + 18f_3(x') - 6\sqrt{3}f_2(x') + 9f_3(x')}{x'^2(1+x')^2(1-x'+x'^2)}{\rm d}x' \\ &\approx -\frac{\Phi_0}{54}\frac{1.845e^{x^{0.104}}}{1+0.563x^{1.158}}\end{aligned} \tag{A15}$$

where the second line is an approximation specifically for UDG1.

B. GC PROFILE: EFF PROFILE

The EFF profile (Elson et al. 1987) is specified by the total mass, $m_{\rm tot}$, the scale length a, and the power-law slope η – the density profile is given by

$$\rho(l) = \frac{\rho_0}{(1+l^2/a^2)^\eta}, \tag{B16}$$

where

$$\rho_0 = \frac{\Gamma(\eta)}{\pi^{3/2}\Gamma(\eta-1)}\frac{m_{\rm tot}}{a^3} \tag{B17}$$

is the central density, with $\Gamma(x)$ the Gamma function.

The enclosed mass of EFF profile is given by

$$m(l) = \frac{4\pi}{3} l^3 \rho_0 \mathcal{F}_{21}\left(\frac{3}{2}, \eta; \frac{5}{2}; -\frac{l^2}{a^2}\right), \tag{B18}$$

where $\mathcal{F}_{21}(a, b; c; z)$ is the hypergeometric function. By solving $m(l) = 0.5 m_{\rm tot}$, one can show that the half-mass radius is given by

$$l_{1/2} = (2^{\frac{2}{2\eta-3}} - 1)^{1/2} a, \tag{B19}$$

a quantity that is repeated used in our model.

As mentioned in Section 2.2, to estimate the tidal heating parameter $f_{\rm t}$, we have we have used the tidal evolution track of Peñarrubia et al. (2010) expressed in terms of the maximum-circular velocity $v_{\rm max}$ and the radius $l_{\rm max}$ at which $v_{\rm max}$ is reached. To this end, we need a relation between $l_{\rm max}$ and the parameters defining the profile, which is obtained as follows. The radius at which the circular velocity reaches maximum, $l_{\rm max}$, is given by the solution of $dv^2_{\rm circ}/dl = 0$, i.e.,

$$\mathcal{F}_{21}\left(\frac{3}{2}, \eta; \frac{5}{2}; -\frac{l^2}{a^2}\right) - \frac{3\eta}{5}\frac{l^2}{a^2}\mathcal{F}_{21}\left(\frac{5}{2}, \eta+1; \frac{7}{2}; -\frac{l^2}{a^2}\right) = 0, \tag{B20}$$

and is well approximated by

$$l_{\rm max} \approx 1.825a \tag{B21}$$

for $\eta = 2$.

C. GC MASS-DISTANCE RELATIONS

As mentioned in Section 2.4, to facilitate parameter inference, we pre-compute the model predictions of the observables used to construct the likelihood using one thousand GCs on a mesh grid spanned by the parameters of interest. We perform linear interpolation for model evaluations during the MCMC run.

Using the tabulated results, we plot the median relations between the evolved GC mass and distance for different halo mass $M_{\rm h}$ and different scale length r_0 of the initial star-cluster distribution, in Figs. 12-13. The concentrations are kept fixed at the posterior mode values, respectively, i.e., Fig. 12 is for NFW halos of $c = 2.8$ and Fig. 13 is for Burkert halos of $c = 14.8$. For the NFW case, we can see clear mass segregation at $M_{\rm h} \lesssim 10^{9.5} M_\odot$ and large r_0. For the Burkert case, mass segregation is achieved at $M_{\rm h} \lesssim 10^{9.0} M_\odot$ and smaller r_0.

REFERENCES

Alexander, P. E. R., & Gieles, M. 2013, MNRAS, 432, L1, doi: 10.1093/mnrasl/slt022

Amorisco, N. C., & Loeb, A. 2016, Monthly Notices of the Royal Astronomical Society: Letters, 459, L51, doi: 10.1093/mnrasl/slw055

Banik, U., & van den Bosch, F. C. 2022, The Astrophysical Journal, 926, 215, doi: 10.3847/1538-4357/ac4242

Bar, N., Danieli, S., & Blum, K. 2022, ApJL, 932, L10, doi: 10.3847/2041-8213/ac70df

Behroozi, P. S., Wechsler, R. H., & Conroy, C. 2013, ApJ, 770, 57, doi: 10.1088/0004-637X/770/1/57

Benavides, J. A., Sales, L. V., Abadi, M. G., et al. 2022, arXiv e-prints, arXiv:2209.07539. https://arxiv.org/abs/2209.07539

Benson, A. J. 2020, MNRAS, 493, 1268, doi: 10.1093/mnras/staa341

Benson, A. J., & Du, X. 2022, MNRAS, 517, 1398, doi: 10.1093/mnras/stac2750

Binney, J., & Tremaine, S. 2008, Galactic Dynamics: Second Edition

Boylan-Kolchin, M., Ma, C., & Quataert, E. 2008, Monthly Notices of the Royal Astronomical Society, 383, 93, doi: 10.1111/j.1365-2966.2007.12530.x

Brown, G., & Gnedin, O. Y. 2021, MNRAS, 508, 5935, doi: 10.1093/mnras/stab2907

Burkert, A. 1995, ApJL, 447, L25, doi: 10.1086/309560

Burkert, A., & Forbes, D. A. 2020, AJ, 159, 56, doi: 10.3847/1538-3881/ab5b0e

Carleton, T., Errani, R., Cooper, M., et al. 2019, Monthly Notices of the Royal Astronomical Society, 485, 382 , doi: 10.1093/mnras/stz383

Chan, T. K. 2019, PhD thesis, University of California, San Diego

Chandrasekhar, S. 1943, ApJ, 97, 255, doi: 10.1086/144517

Danieli, S., Dokkum, P. v., Conroy, C., Abraham, R., & Romanowsky, A. J. 2019, The Astrophysical Journal Letters, 874, L12, doi: 10.3847/2041-8213/ab0e8c

Danieli, S., Greene, J. E., Carlsten, S., et al. 2022a, arXiv e-prints, arXiv:2210.14233. https://arxiv.org/abs/2210.14233

Danieli, S., van Dokkum, P., Trujillo-Gomez, S., et al. 2022b, ApJL, 927, L28, doi: 10.3847/2041-8213/ac590a

Di Cintio, A., Brook, C. B., Dutton, A. A., et al. 2017, MNRAS, 466, L1, doi: 10.1093/mnrasl/slw210

Diemer, B., & Kravtsov, A. V. 2015, ApJ, 799, 108, doi: 10.1088/0004-637X/799/1/108

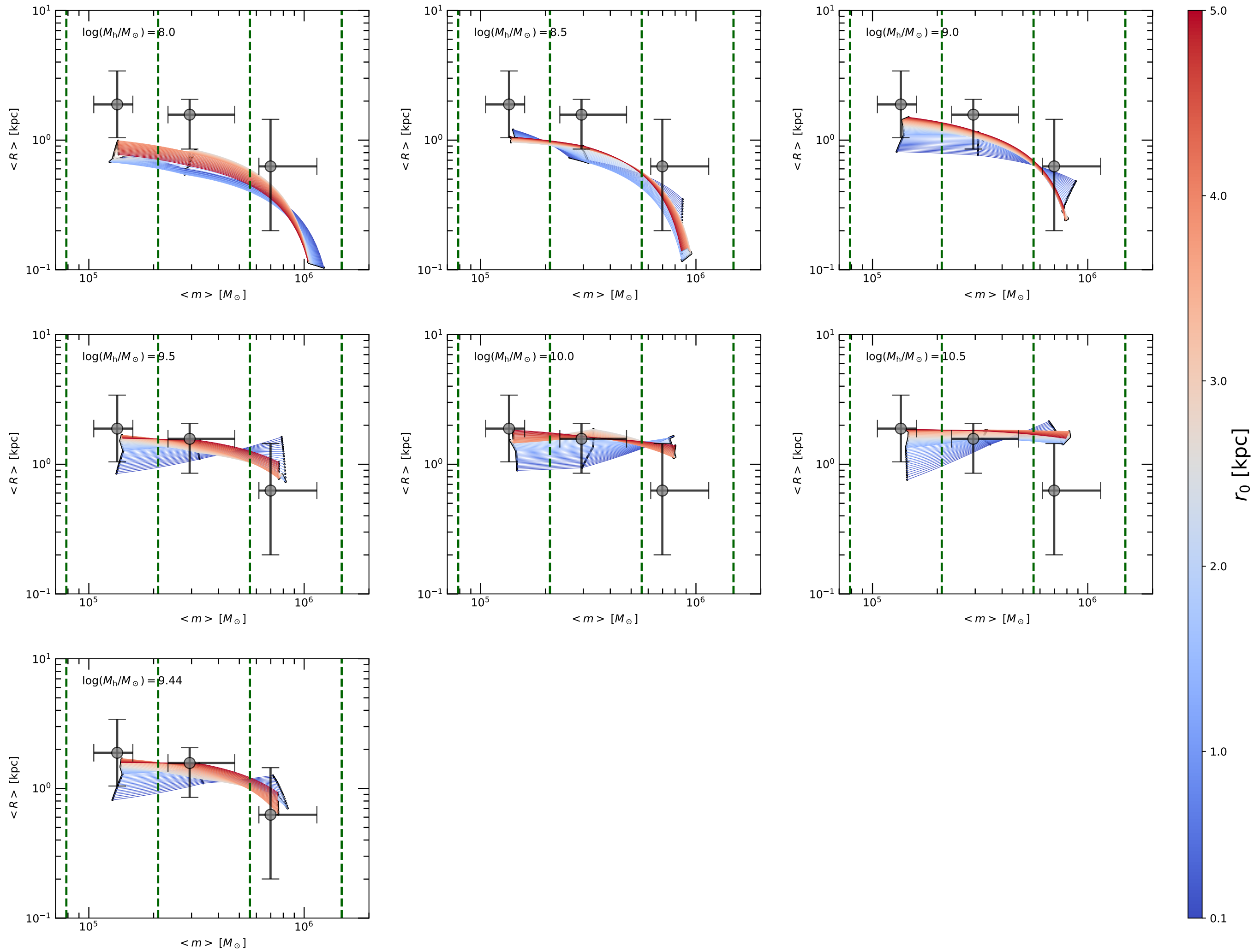

Figure 12. The median galactocentric distance $\langle R \rangle$ versus the median GC mass $\langle m \rangle$, in three mass bins, for different host halo masses (M_h) and different scale distance of the initial star-cluster distribution (r_0). The green dashed lines stand for the boundaries of the mass bins. The gray circles represent the data with the error bars indicating the 16th and 84th percentiles (the same across panels). The lines are model realizations for NFW halos with concentration $c = 2.8$ fixed. The last panel shows the results corresponding to the posterior-mode halo mass.

Dutta Chowdhury, D., van den Bosch, F. C., & van Dokkum, P. 2020, ApJ, 903, 149, doi: 10.3847/1538-4357/abb947

Dutton, A. A., & Macciò, A. V. 2014, MNRAS, 441, 3359, doi: 10.1093/mnras/stu742

Elson, R. A. W., Fall, S. M., & Freeman, K. C. 1987, ApJ, 323, 54, doi: 10.1086/165807

Forbes, D. A., Alabi, A., Romanowsky, A. J., Brodie, J. P., & Arimoto, N. 2020, Monthly Notices of the Royal Astronomical Society, 492, 4874, doi: 10.1093/mnras/staa180

Forbes, D. A., Gannon, J. S., Romanowsky, A. J., et al. 2021, MNRAS, 500, 1279, doi: 10.1093/mnras/staa3289

Forbes, D. A., Read, J. I., Gieles, M., & Collins, M. L. M. 2018, MNRAS, 481, 5592, doi: 10.1093/mnras/sty2584

Foreman-Mackey, D., Hogg, D. W., Lang, D., & Goodman, J. 2013, PASP, 125, 306, doi: 10.1086/670067

Freundlich, J., Dekel, A., Jiang, F., et al. 2020, MNRAS, 491, 4523, doi: 10.1093/mnras/stz3306

Gan, J., Kang, X., van den Bosch, F. C., & Hou, J. 2010, MNRAS, 408, 2201, doi: 10.1111/j.1365-2966.2010.17266.x

Gieles, M., Heggie, D. C., & Zhao, H. 2011, MNRAS, 413, 2509, doi: 10.1111/j.1365-2966.2011.18320.x

Gieles, M., & Renaud, F. 2016, MNRAS, 463, L103, doi: 10.1093/mnrasl/slw163

Goerdt, T., Moore, B., Read, J. I., Stadel, J., & Zemp, M. 2006, MNRAS, 368, 1073, doi: 10.1111/j.1365-2966.2006.10182.x

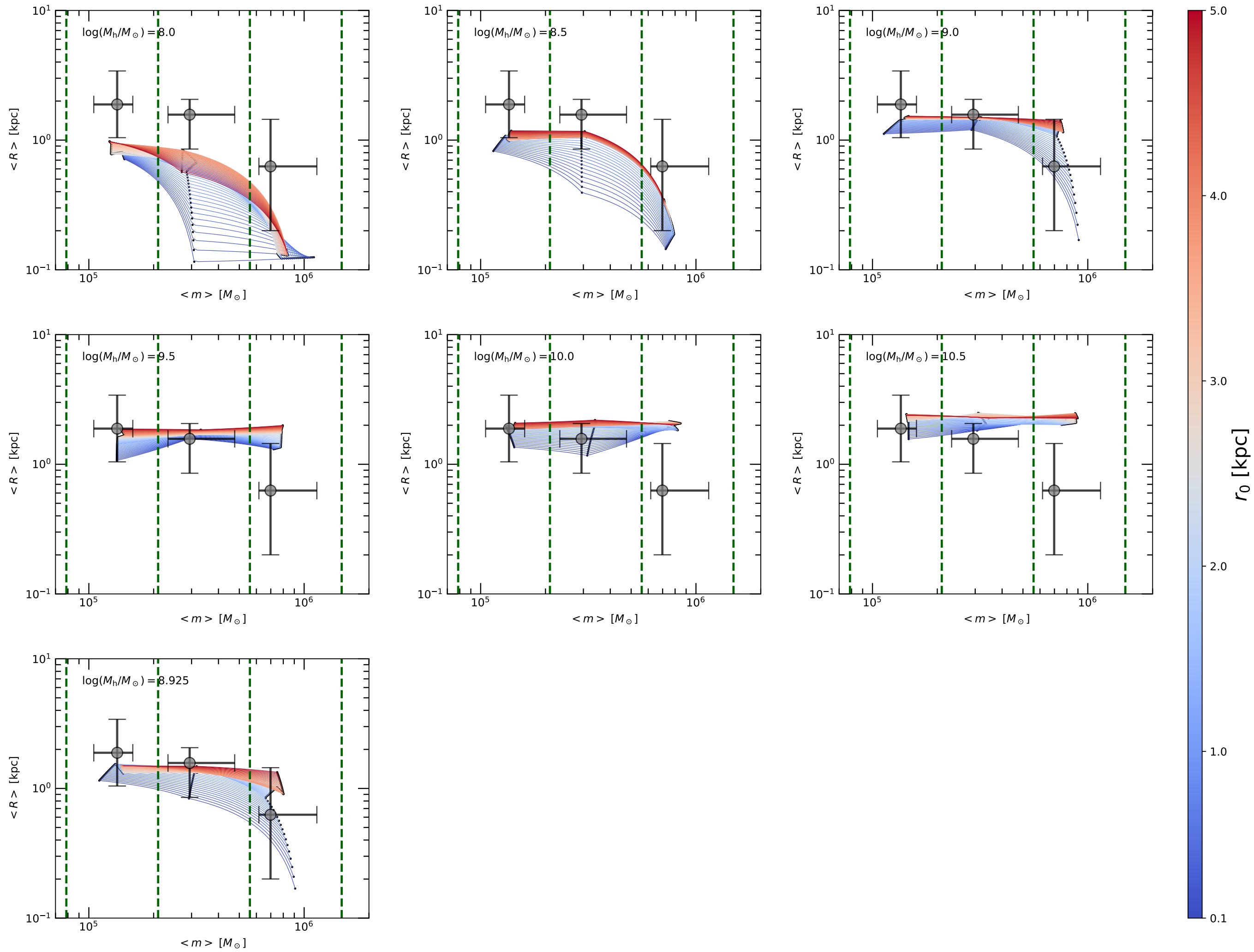

Figure 13. The same as Fig. 12, but for Burkert halos with $c = 14.8$.

Greco, J. P., Greene, J. E., Strauss, M. A., et al. 2018, ApJ, 857, 104, doi: 10.3847/1538-4357/aab842

Green, S. B., van den Bosch, F. C., & Jiang, F. 2021, MNRAS, 503, 4075, doi: 10.1093/mnras/stab696

Guo, Q., Hu, H., Zheng, Z., et al. 2020, Nature Astronomy, 4, 246, doi: 10.1038/s41550-019-0930-9

Harris, W. E., Blakeslee, J. P., & Harris, G. L. H. 2017, ApJ, 836, 67, doi: 10.3847/1538-4357/836/1/67

Harris, W. E., Harris, G. L., & Hudson, M. J. 2015, ApJ, 806, 36, doi: 10.1088/0004-637X/806/1/36

Hénon, M. 1965, Annales d'Astrophysique, 28, 992

Hernquist, L. 1990, ApJ, 356, 359, doi: 10.1086/168845

Hudson, M. J., Harris, G. L., & Harris, W. E. 2014, ApJL, 787, L5, doi: 10.1088/2041-8205/787/1/L5

Inoue, S. 2009, MNRAS, 397, 709, doi: 10.1111/j.1365-2966.2009.15066.x

Iodice, E., Cantiello, M., Hilker, M., et al. 2020, A&A, 642, A48, doi: 10.1051/0004-6361/202038523

Jiang, F., Dekel, A., Freundlich, J., et al. 2019, MNRAS, 487, 5272, doi: 10.1093/mnras/stz1499

—. 2021, MNRAS, 502, 621, doi: 10.1093/mnras/staa4034

Jiang, F., & van den Bosch, F. C. 2017, Monthly Notices of the Royal Astronomical Society, 472, 657 , doi: 10.1093/mnras/stx1979

Just, A., Khan, F. M., Berczik, P., Ernst, A., & Spurzem, R. 2011, MNRAS, 411, 653, doi: 10.1111/j.1365-2966.2010.17711.x

Kaur, K., & Sridhar, S. 2018, ApJ, 868, 134, doi: 10.3847/1538-4357/aaeacf

King, I. 1962, AJ, 67, 471, doi: 10.1086/108756

Lamers, H. J. G. L. M., Baumgardt, H., & Gieles, M. 2010, MNRAS, 409, 305, doi: 10.1111/j.1365-2966.2010.17309.x

Liao, S., Gao, L., Frenk, C. S., et al. 2019, MNRAS, 490, 5182, doi: 10.1093/mnras/stz2969

Lim, S., Peng, E. W., Côté, P., et al. 2018, ApJ, 862, 82, doi: 10.3847/1538-4357/aacb81

Marleau, F. R., Habas, R., Poulain, M., et al. 2021, A&A, 654, A105, doi: 10.1051/0004-6361/202141432

Modak, S., Danieli, S., & Greene, J. E. 2022, arXiv, doi: 10.48550/arxiv.2211.01384

Moreno, J., Danieli, S., Bullock, J. S., et al. 2022, Nature Astronomy, 6, 496, doi: 10.1038/s41550-021-01598-4

Müller, O., Marleau, F. R., Duc, P.-A., et al. 2020, A&A, 640, A106, doi: 10.1051/0004-6361/202038351

Navarro, J. F., Frenk, C. S., & White, S. D. M. 1997, ApJ, 490, 493, doi: 10.1086/304888

Peñarrubia, J., Benson, A. J., Walker, M. G., et al. 2010, MNRAS, 406, 1290, doi: 10.1111/j.1365-2966.2010.16762.x

Petts, J. A., Gualandris, A., & Read, J. I. 2015, MNRAS, 454, 3778, doi: 10.1093/mnras/stv2235

Petts, J. A., Read, J. I., & Gualandris, A. 2016, MNRAS, 463, 858, doi: 10.1093/mnras/stw2011

Quinlan, G. D. 1996, NewA, 1, 255, doi: 10.1016/S1384-1076(96)00018-8

Read, J. I., Goerdt, T., Moore, B., et al. 2006, MNRAS, 373, 1451, doi: 10.1111/j.1365-2966.2006.11022.x

Rong, Y., Guo, Q., Gao, L., et al. 2017, MNRAS, 470, 4231, doi: 10.1093/mnras/stx1440

Ryon, J. E., Bastian, N., Adamo, A., et al. 2015, Monthly Notices of the Royal Astronomical Society, 452, doi: 10.1093/mnras/stv1282

Sales, L. V., Navarro, J. F., Peñafiel, L., et al. 2020, MNRAS, 494, 1848, doi: 10.1093/mnras/staa854

Silk, J. 2017, ApJL, 839, L13, doi: 10.3847/2041-8213/aa67da

Spitzer, L. 1987, Dynamical evolution of globular clusters

Sánchez-Janssen, R., Côté, P., Ferrarese, L., et al. 2019, The Astrophysical Journal, 878, 18, doi: 10.3847/1538-4357/aaf4fd

Tremmel, M., Wright, A. C., Brooks, A. M., et al. 2020, MNRAS, 497, 2786, doi: 10.1093/mnras/staa2015

Trujillo-Gomez, S., Reina-Campos, M., & Kruijssen, J. M. D. 2019, MNRAS, 488, 3972, doi: 10.1093/mnras/stz1932

van Dokkum, P., Danieli, S., Abraham, R., Conroy, C., & Romanowsky, A. J. 2019, ApJL, 874, L5, doi: 10.3847/2041-8213/ab0d92

van Dokkum, P., Abraham, R., Brodie, J., et al. 2016, ApJL, 828, L6, doi: 10.3847/2041-8205/828/1/L6

van Dokkum, P., Abraham, R., Romanowsky, A. J., et al. 2017, ApJL, 844, L11, doi: 10.3847/2041-8213/aa7ca2

van Dokkum, P., Danieli, S., Cohen, Y., et al. 2018, Nature, 555, 629, doi: 10.1038/nature25767

van Dokkum, P., Shen, Z., Keim, M. A., et al. 2022, Nature, 605, 435, doi: 10.1038/s41586-022-04665-6

Wechsler, R. H., Bullock, J. S., Primack, J. R., Kravtsov, A. V., & Dekel, A. 2002, ApJ, 568, 52, doi: 10.1086/338765

Zentner, A. R., & Bullock, J. S. 2003, ApJ, 598, 49, doi: 10.1086/378797